JACS
JOURNAL OF THE AMERICAN CHEMICAL SOCIETY

pubs.acs.org/JACS

Article

# NIR-Switched DNA Shutter Enables Reversible Intermittent cGAS-STING Activation for Enhanced Antitumor Immunity

Shiyi Bi, Ruowen Yang, Yulin Cong, Huangxian Ju, and Ying Liu*

Cite This: *J. Am. Chem. Soc.* 2025, 147, 30989−31003

Read Online

ACCESS | Metrics & More | Article Recommendations | Supporting Information

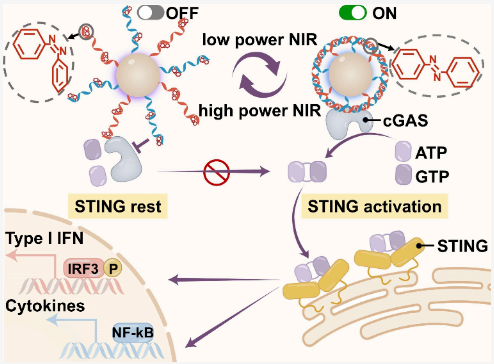

**ABSTRACT:** With their remarkable activation efficiency, cGAS-STING agonists have emerged as a promising strategy to promote immunotherapy. However, continuous activation of the STING pathway may induce resistance and immune evasion, thus impairing the therapeutic effect. Considering repetitive transient rest could restore immune system function and avoid side effects, here we develop an intermittent STING agonist to reversibly activate the cGAS-STING pathway with "stimulation-suspension" patterns, which induce repetitive "activation-rest" intervals in immunotherapy with enhanced efficiency. Near infrared (NIR) switchable reversible DNA shutter (NIR-DNA shutter), as the intermittent STING agonist, is synthesized by conjugating a pair of segmented complementary DNA strands that incorporated Azobenzene (Azo) to the surface of upconversion nanoparticles (UCNPs). Low power 808 nm irradiation generates a high Vis/UV ratio for UCNPs upconversion emission, which induces *trans*-Azo isomerization and assembles dsDNA chain along UCNPs surface to activate STING pathway, while high power 808 nm irradiation generates a high UV/Vis ratio for UCNPs upconversion emission, which induces *cis*-Azo isomerization and disassembles dsDNA chain to pause STING pathway. Switching NIR irradiation powers reversibly converts the NIR-DNA shutter between "ON/OFF" statuses and programs the cGAS-STING pathway with repetitive "activation-rest" interval mode, which demonstrates superior therapeutic efficacy by remodeling the immune-environment and enhancing tumor cell killing compared with the constant STING agonist.

## INTRODUCTION

Cyclic guanosine monophosphate-adenosine monophosphate synthetase (cGAS) - stimulator of interferon gene (STING) is an important innate immune pathway that promotes antitumor immunity.[1−3] The enzymatic function of cGAS is activated upon binding to double-stranded DNA (dsDNA) in a sequence-independent manner, enabling it to catalyze synthesis of the second messenger cyclic GMP-AMP (cGAMP). cGAMP then binds to STING and activates downstream signaling pathways with a series of cytokines release, which ultimately endows the body with a powerful antitumor immune force.[4,5] STING agonists have emerged as a promising strategy for reinvigorating antitumor immunity,[1,6,7] which include small molecules such as 4-(5,6-dimethoxybenzo[b]thiophen-2-yl)-4-oxobutanoic acid (MSA-2) that binds to STING,[8] cyclic dinucleotides (CDNs) that mimic endogenous cGAMP,[9] and metal ions ($Zn^{2+}$, $Mn^{2+}$)[10] that enhance cGAS activity, as well as polypeptides that induce STING assembly.[11]

Despite their remarkable activation efficiency, currently reported STING agonists still lack control over the operation location and duration. Improper activation of immune signaling pathways may lead to off-tumor toxicity and autoimmune disorders.[12,13] Overactivation by STING agonists can promote immunosuppressive microenvironment formation,[14] damage T cells by inducing apoptosis, and compromise outcomes of immunotherapies.[15,16] Moreover, continuous stimulation of the cGAS-STING pathway causes severe inflammatory conditions, which may promote immune evasion and metastasis.[17] Since transient rest could restore the functionality of the immune system,[18] "activation-rest" intervals have been generated in immunotherapy by repetitive invasive administrations of small-molecule inhibitors for efficiency enhancement.[19] Therefore, developing intermittent STING agonists that manipulate the cGAS-STING pathway with "activation-rest" intervals in a facile and noninvasive mode would be highly desired.

DNA is highly programmable based on Watson−Crick base pairing, which exhibits advantages of precise structure and configuration controls.[20] Long dsDNA with over 40 base pairs[21,22] would provide a more stable cGAS-DNA complex with more efficient STING activation. Therefore, hairpin structured DNA strands have been reported as STING agonists to generate dsDNA chain intracellularly.[23,24] By integrating single or dual cleavable points that respond to

**Received:** May 21, 2025
**Revised:** August 8, 2025
**Accepted:** August 8, 2025
**Published:** August 18, 2025

https://doi.org/10.1021/jacs.5c08583

**Scheme 1. Schematic Illustration of NIR-DNA Shutter As Intermittent STING Agonist to Enhance Immunotherapy with "Activation-Rest" Intervals**[a]

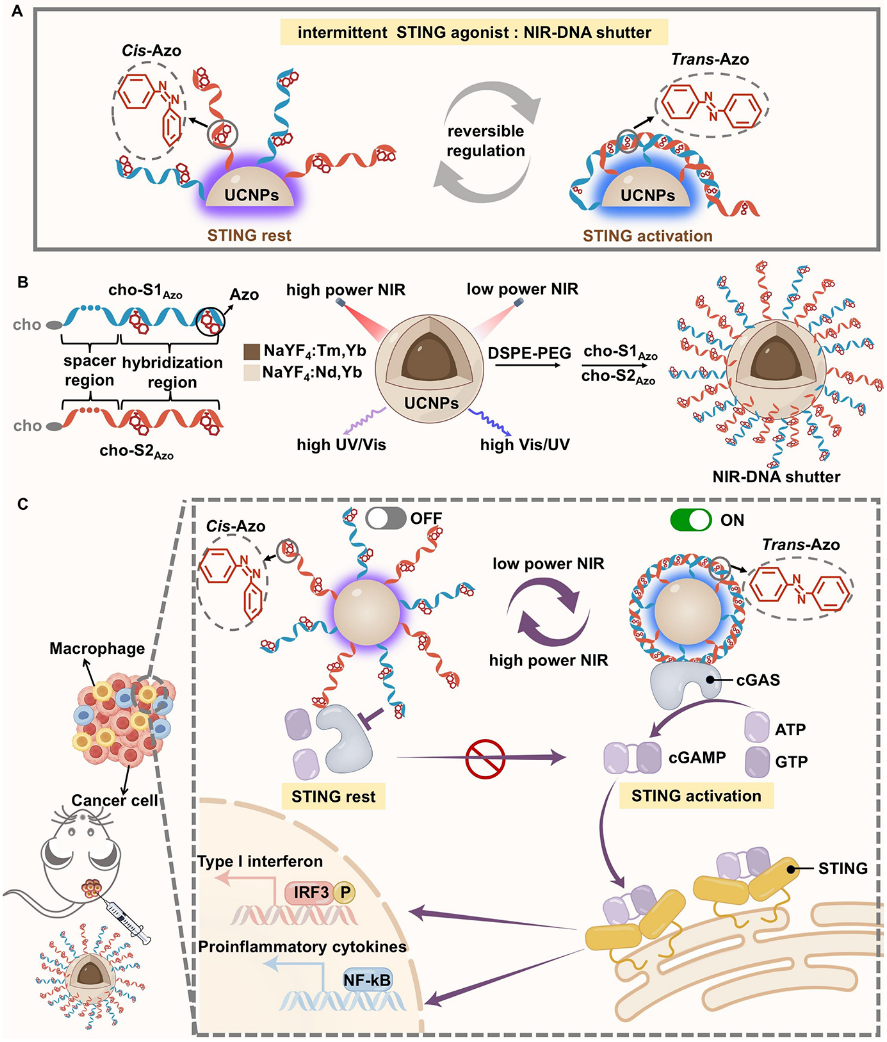

[a](A) NIR-DNA shutter as intermittent STING agonist with reversible STING "activation-rest" regulation. (B) Synthesis of NIR-DNA shutter. (C) NIR-switched DNA shutter as an intermittent STING agonist for reversible regulation of the cGAS-STING pathway.

stimuli, including UV exposure or endonuclease, into hairpin DNA strands, cGAS-STING pathway activation or termination has been regulated in a "one-way" mode.[25,26] Although demonstrating impressive manipulation of the STING pathway, the as-reported "one-way" STING agonists are incapable of performing repetitive reversible "activation-rest" intervals in STING pathway regulations. In addition, dependence on UV light as a stimulus further impedes its potential for in vivo applications considering the limited tissue penetration depth.

To achieve immunotherapy boosting with "activation-rest" intervals, here we develop a near-infrared (NIR)-switched DNA shutter (NIR-DNA shutter) as an intermittent STING agonist, which programs the cGAS-STING pathway with a reversible regulation mode via an Azobenzene (Azo) trigger for programming dsDNA chain hybridization and dehybridization along the upconversion nanoparticle (UCNPs) surface (Scheme 1A). To prepare the NIR-DNA shutter, a pair of photoswitchable DNA strands, cho-S1$_{Azo}$ and cho-S2$_{Azo}$, is designed as components for the dsDNA chain. Cho-S1$_{Azo}$/cho-S2$_{Azo}$ strands both consist of an 18-base hybridization region and a 15-base poly-T spacer region and are functionalized with cholesterol at 5′ and 3′ termini, respectively, for anchoring to UCNPs surface. The hybridization regions of cho-S1$_{Azo}$/cho-S2$_{Azo}$ are segmented complementary to allow their sequential hybridization for the generation of a long dsDNA chain. Four pairs of Azo groups, which switch between *cis* and *trans* isomerizations upon UV/Vis exposure, respectively,[27−29] were introduced into the hybridization regions of both strands to achieve photoswitched hybridization and dehybridization of a long dsDNA chain (Scheme 1B, cho-S1$_{Azo}$, cho-S2$_{Azo}$). Core–shell UCNPs $NaYF_4$:Tm,Yb@$NaYF_4$:Nd,Yb are synthesized as miniature light transducers to upconvert 808 nm NIR excitation to UV/Vis emissions at 450/475 and 343/365 nm respectively, while low power 808 nm irradiation results in high Vis/UV emission ratio and high power 808 nm irradiation results in high UV/Vis emission ratio (Scheme 1B, UCNPs). UCNPs are covered with DSPE-PEG on the surface, and anchored with cho-S1$_{Azo}$, cho-S2$_{Azo}$ strands via hydrophobic–hydrophobic interactions between cholesterol and DSPE to obtain NIR-DNA shutter as an intermittent agonist for cGAS-STING pathway regulation with "activation-rest" intervals (Scheme 1B, NIR-DNA shutter).

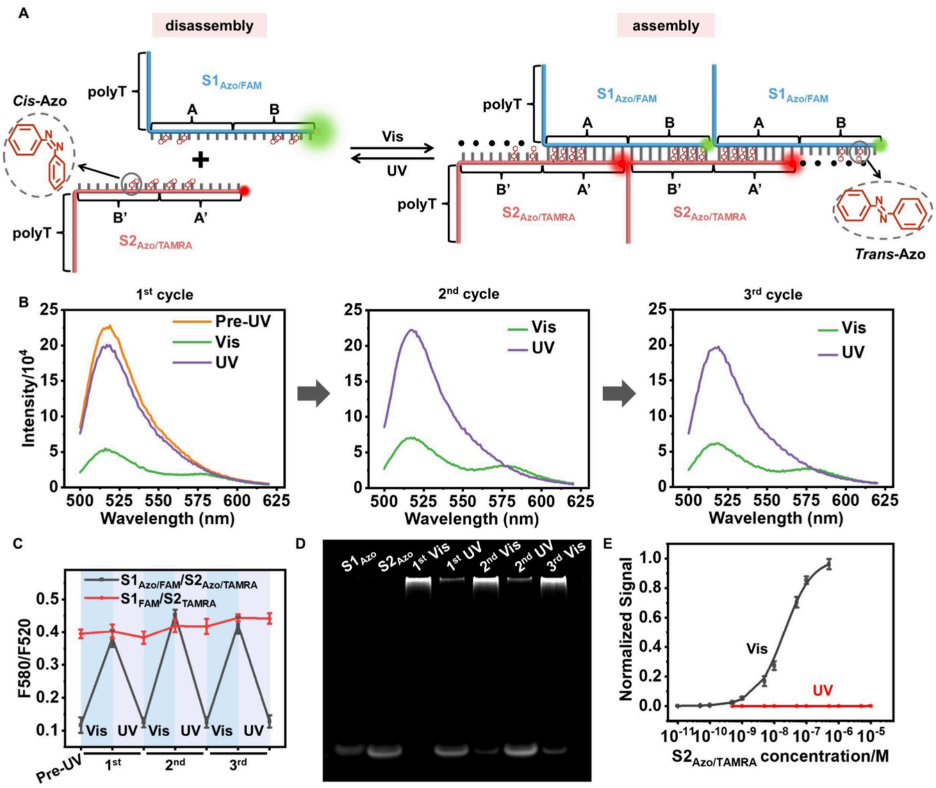

**Figure 1.** Synthesis of dsDNA chain and its reversible photo responses. (A) Schematic illustration of $S1_{Azo/FAM}$, $S2_{Azo/TAMRA}$ structures and optically switched dsDNA chain assembly and disassembly. (B) Fluorescence spectra of $S1_{Azo/FAM}/S2_{Azo/TAMRA}$ under three cycles of alternate Vis/UV irradiations and corresponding (C) fluorescence intensity ratios of TAMRA and FAM (F580/F520) for "reversible" group $S1_{Azo/FAM}/S2_{Azo/TAMRA}$ and "unreversible" control group $S1_{FAM}/S2_{TAMRA}$. (D) PAGE characterization of $S1_{Azo}/S2_{Azo}$ under alternate Vis/UV irradiations. (E) Normalized fluorescence signal plotted as a function of $S2_{Azo/TAMRA}$ concentration with fitting.

For in vivo manipulation of the cGAS-STING pathway, the NIR-DNA shutter is intratumorally injected into tumor-bearing mice, which is subsequently exposed to alternative low power and high power 808 nm irradiations. Under low power NIR irradiation, a high Vis/UV emission ratio switches Azo to *trans-* isomerization and promotes the assembly of long dsDNA chain along the UCNPs surface via sequential hybridization of $S1_{Azo}$ and $S2_{Azo}$. The assembly of dsDNA turns on the NIR-DNA shutter (Scheme 1C, "ON" status), which allows cGAS binding and produces cGAMP using adenosine triphosphate (ATP) and guanosine triphosphate (GTP) as substrates. The as-generated cGAMP then activates STING and triggers the release of a series of immune stimulators, such as type I interferons (IFN-I), to activate T cells by enhancing antigen presentation and providing costimulatory signals. The poly-T spacer region saves space around a long dsDNA chain, which not only guarantees $S1_{Azo}$/$S2_{Azo}$ hybridization efficiency along the UCNPs surface, but also allows efficient cGAS binding to dsDNA. In addition, the fastening of cho-$S1_{Azo}$, cho-$S2_{Azo}$ strands on UCNPs' surface enhances their high local concentrations, and the corresponding generation of dsDNA chain along UCNPs with a net-like structure provides higher valency for cGAS-STING complex with enhanced enzymatic activity. Under high power NIR irradiation, a high UV/Vis emission ratio switches Azo to *cis-*isomerization, which disassembles the long dsDNA chain, and correspondingly turns off the NIR-DNA shutter to pause the cGAS-STING pathway (Scheme 1C, "OFF" status). Therefore, switching 808 nm excitation light between low power and high power drives reversible "ON-OFF" status conversion of NIR-DNA shutter, which manipulates cGAS-STING pathway with "activation-rest" intervals. The intermittent modulation strategy demonstrates superior therapeutic efficacy by reducing immunosuppressive cells in the tumor microenvironment and elevating $CD4^+$ helper T cells and $CD8^+$ cytotoxic T cell levels. Compared with the constant STING agonist, the as-reported intermittent STING agonist effectively enhances tumor cell killing by immune cells and suppresses tumor growth.

## ■ RESULTS AND DISCUSSION

**Photoswitched dsDNA Chain Assembly and Disassembly.** To verify the assembly of the dsDNA chain, DNA strands S1 and S2 that consist of an 18-nt hybridization region and a 15-nt poly-T spacer region, respectively, were prepared. DNA strand S1 has a spacer region in its 5′ terminus and segments A, B for the hybridization region in its 3′ terminus. DNA strand S2 has a spacer region in its 3′ terminus and segments B', A' for the hybridization region in its 5′ terminus. Segments A and B in S1 have complementary sequences to segments A' and B' in S2, thus could alternately hybridize to generate a long dsDNA chain with repeating hybridization units AA'/BB' (Figure S1A). The successful assembly of a long dsDNA chain was confirmed using polyacrylamide gel electrophoresis (PAGE), which showed a single band with significantly lower mobility after incubating S1 and S2 for 30 min at 37 °C (Figure S1B, lane 3). Atomic force microscopy (AFM) images revealed a linear DNA strand approximately 1.5 nm in height, consistent with the expected height of double-stranded DNA (Figure S1C), further confirming the successful

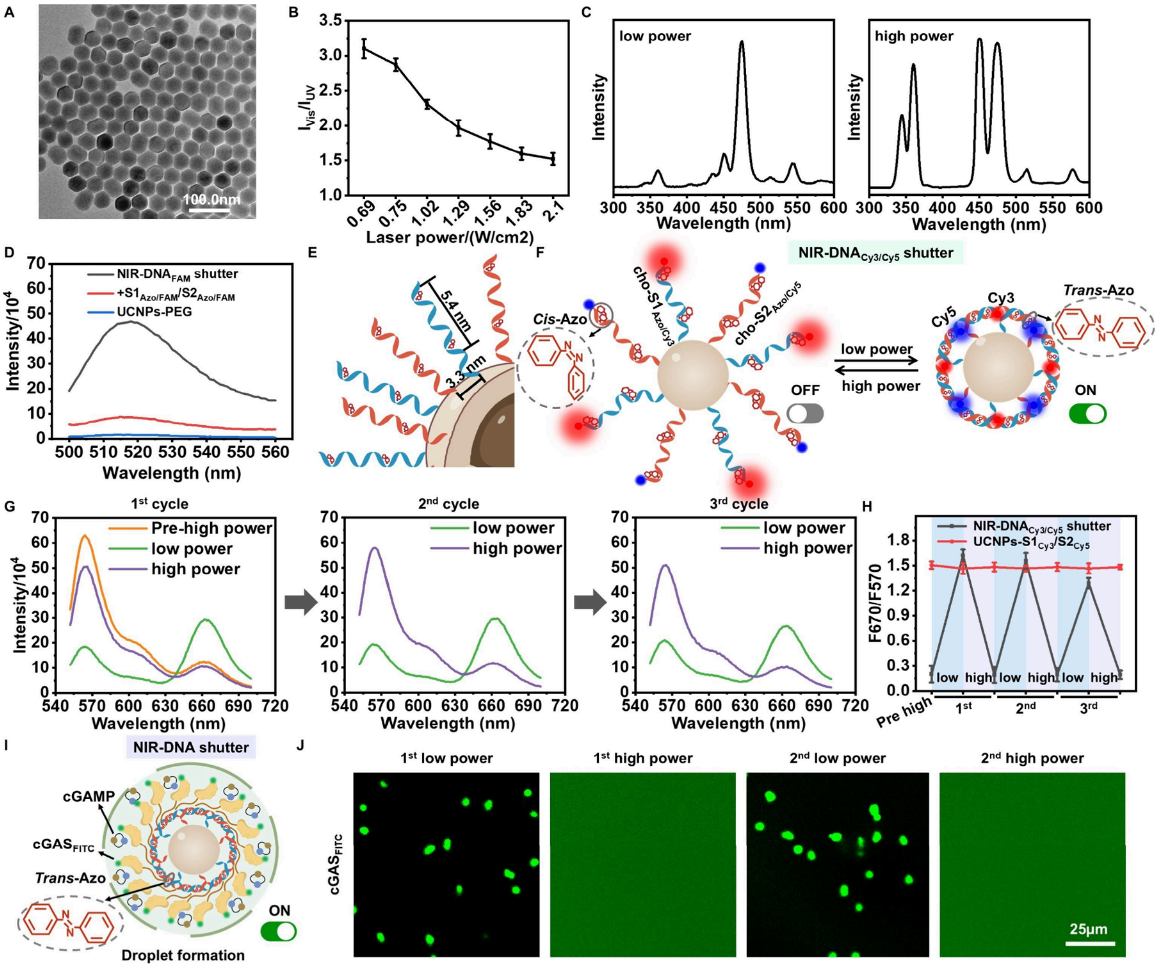

**Figure 2.** Synthesis of NIR-DNA shutter and its reversible status "ON/OFF" switch upon low power and high power 808 nm excitation. (A) TEM images of UCNPs. (B) Vis over UV emission intensity ratio ($I_{Vis}/I_{UV}$) of UCNPs in response to different power density of 808 nm excitation laser. (C) Emission spectra of UCNPs upon low power density (0.75 W/cm$^2$) and high power density (2.10 W/cm$^2$) 808 nm NIR irradiation. (D) Fluorescence spectra of UCNPs-PEG, UCNPs-PEG mixed with S1$_{Azo/FAM}$/S2$_{Azo/FAM}$ (+S1$_{Azo/FAM}$/S2$_{Azo/FAM}$), and NIR-DNA$_{FAM}$ shutter. Schematic illustrations of (E) cho-S1$_{Azo}$, cho-S2$_{Azo}$ distribution on UCNPs surface and (F) reversible status conversion of NIR-DNA$_{Cy3/Cy5}$ shutter upon low and high NIR irradiation powers. (G) Fluorescence spectra of NIR-DNA shutter under three cycles of alternate low/high power 808 nm irradiations, and corresponding (H) fluorescence intensity ratios of Cy5 and Cy3 (F670/F570) for NIR-DNA$_{Cy3/Cy5}$ shutter, constant STING agonist control group UCNPs-S1$_{Cy3}$/S2$_{Cy5}$ under different power 808 nm laser irradiation. (I) Schematic illustration of FITC florescent droplet-like structure formation with "ON" status NIR-DNA shutter and (J) its corresponding phase separation characterization in response to two cycles of alternate low power/high power 808 nm laser irradiation.

generation of long dsDNA via alternative hybridization of S1 and S2.

As a photodriven trigger that switches between two isomerizations for operating molecular machines[30−32] and manipulating DNA hybridization/dehybridization,[29,33−37] azobenzene (Azo) was incorporated into the backbone of S1/S2 for photo-switched assembly and disassembly of dsDNA chain (S1$_{Azo}$/S2$_{Azo}$). S1$_{Azo}$ contains two Azo molecules between the 2/3 base and the 4/5 base in segment A and two Azo molecules between the 5/6 base and the 7/8 base in segment B respectively, and S2$_{Azo}$ contains two Azo molecules between the 6/7 base and the 8/9 base in segments A' and two Azo molecules between the 1/2 base and the 3/4 base in B' respectively. Azo molecules are located in pairs with one base in between, which generates four pairs of Azo occupied each repeating hybridization unit AA'/BB' in the dsDNA chain. The 3′ terminus and 5′ terminus of S1$_{Azo}$ and S2$_{Azo}$ were labeled with FAM and TAMRA, respectively (Figure 1A, S1$_{Azo/FAM}$, S2$_{Azo/TAMRA}$) for fluorescence characterization of photo-switched assembly/disassembly transitions of the dsDNA chain. Visible light (450 nm, 14 mW/cm$^2$) keeps the planar *trans*-isomer of Azo, thus stabilizing the duplex structure of dsDNA by stacking with adjacent base pairs. UV light (365 nm, 6 mW/cm$^2$) converts Azo to its nonplanar *cis*-isomer, thus dehybridizing the duplex structure of dsDNA through steric hindrance. This light-switched isomerization conversion of Azo reversibly programs the assembly and disassembly of the dsDNA chain (Figure 1A).

To alternatively switch the assembly and disassembly of the dsDNA chain, S1$_{Azo/FAM}$ and S2$_{Azo/TAMRA}$ were pretreated with UV light to make Azo in *Cis* isomerization that is unfavorable for DNA hybridization, which only showed FAM fluorescence at 520 nm upon 488 nm excitation (Figure 1B, Pre-UV). The assembly of dsDNA upon Vis irradiation resulted in proximity of FAM and TAMRA with efficient Förster resonance energy transfer (FRET) process from FAM to TAMRA (Figure 1B, 1st cycle, Vis) and corresponding increase of TAMRA/FAM fluorescence ratio (F580/F520) (Figure 1C, S1$_{Azo/FAM}$/

$S2_{Azo/TAMRA}$, 1st, Vis). Subsequent UV irradiation recovered FAM fluorescence intensity at 520 nm (Figure 1B, 1st cycle, UV) with a significant decrease of F580/F520 (Figure 1C, $S1_{Azo/FAM}/S2_{Azo/TAMRA}$, 1st, UV), indicating efficient disassembly of dsDNA. The alternate Vis/UV irradiations were repeated for three cycles, and demonstrated consistent FRET (F580/F520) signal switches across irradiation cycles (Figure 1B, 2nd cycle, 3rd cycle, Figure 1C, $S1_{Azo/FAM}/S2_{Azo/TAMRA}$, 2nd, 3rd), indicating efficient photoprogrammed reversible dsDNA chain assembly and disassembly. However, fewer Azo modifications failed to induce complete dsDNA dehybridization (Figure S2). $S1_{FAM}/S2_{TAMRA}$, in the absence of Azo modification, were set as "unreversible" control group, which produced a dsDNA chain upon the mixture of $S1_{FAM}$ and $S2_{TAMRA}$ and remained hybridized regardless of alternate Vis/UV irradiations with high FRET (F580/F520) signal (Figures S3 and 1C, $S1_{FAM}/S2_{TAMRA}$). The reversible assembly/disassembly of the dsDNA chain was further confirmed by native polyacrylamide gel electrophoresis (PAGE) characterization. Under visible light irradiation, the PAGE bands demonstrated much lower mobility compared with single-stranded DNA ($S1_{Azo}/S2_{Azo}$) bands, indicating successful formation of the dsDNA chain (Figure 1D, 1st Vis). UV irradiation restored bands to positions corresponding to dissociated $S1_{Azo}/S2_{Azo}$ (Figure 1D, 1st UV). Alternate Vis/UV irradiations were repeated and demonstrated reversible PAGE patterns that aligned with the 1st cycle of Vis/UV irradiations (Figure 1D, 2nd Vis, 2nd UV, 3rd Vis).

To compare the hybridization tendencies of $S1_{Azo}$ and $S2_{Azo}$ with Azo in *Cis* and *Trans* isomerizations, respectively, the dissociation constants ($K_d$) were determined by fluorescence FRET assays using $S1_{Azo/FAM}$ and $S2_{Azo/TAMRA}$. Serial dilutions of $S2_{Azo/TAMRA}$ were incubated with a fixed concentration of $S1_{Azo/FAM}$ until equilibrium was reached. Fluorescence intensities were measured to calculate the fraction of hybridized DNA, and $K_d$ values were derived by fitting the data to the Langmuir isotherm equation model. Nonlinear curve fitting analysis revealed a $K_d$ value of ~20.20 nM for $S1_{Azo}$ and $S2_{Azo}$ under visible irradiation with *trans*-Azo (Figure 1E, Vis), whereas hybridization was hardly achieved for $S1_{Azo}$ and $S2_{Azo}$ under UV irradiation with *cis*-Azo in the tested concentration range (Figure 1E, UV). The nM range of $K_d$ value indicated the structure stability of the dsDNA chain under Vis irradiation,[38] and these results further demonstrated the high efficiency of photomodulated dsDNA chain assembly/disassembly processes.

**Synthesis and Characterization of NIR-DNA Shutter UCNPs-$S1_{Azo}/S2_{Azo}$.** Considering the limited tissue penetrations of UV/Vis irradiations, upconversion nanoparticles (UCNPs) that upconvert NIR irradiation to UV/Vis emissions were introduced to reversibly switch dsDNA chain assembly and disassembly. NIR-DNA shutter UCNPs-$S1_{Azo}/S2_{Azo}$ was accordingly prepared as an intermittent STING agonist. The core−shell structured UCNPs $NaYF_4$:Tm,Yb@$NaYF_4$:Nd,Yb, consisting of an activator $Tm^{3+}$ doped upconversion core $NaYF_4$:0.5%$Tm^{3+}$,30%$Yb^{3+}$ and a sensitizer $Nd^{3+}$ doped NIR absorption shell $NaYF_4$:10%$Nd^{3+}$,10%$Yb^{3+}$, was synthesized using our previously reported method,[39] and showed monodisperse particle sizes for UCNPs core of 31.5 ± 1.85 nm (Figure S4) and for core−shell UCNPs of 41.6 ± 2.13 nm (Figure 2A). $Nd^{3+}$ sensitizer in the shell absorbed 808 nm NIR light irradiation and transferred energy to $Tm^{3+}$ in the core through $Yb^{3+}$, which produced upconversion peaks corresponding to the $^1I_6 \gg {}^3F_4$ and $^1D_2 \gg {}^3H_6$ transitions in UV region at 343 and 365 nm respectively, and $^1D_2 \gg {}^3F_4$ and $^1G_4 \gg {}^3H_6$ transitions in Vis region at 450 and 475 nm, respectively. Notably, the intensity ratio of upconverted UV/Vis luminescence is highly dependent on the power density of the excitation light (Figure S5). Considering the saturation of Vis emissions at high excitation powers,[40] the Vis/UV luminescence intensity ratio decreases as the power density of 808 nm excitation light increases (Figure 2B). At a low power density of 0.75 W/cm$^2$, UCNPs predominantly generated Vis emission with a Vis/UV intensity ratio of 2.87 (Figure 2C, low power), while the ratio decreased to 1.52 at a high power density of 2.10 W/cm$^2$ (Figure 2C, high power). The successful excitation power-dependent manipulation of UCNPs' upconversion emission intensity ratio endowed it with the capability of Azo isomerization switching.

The synthesized oleic acid (OA)-capped UCNPs were modified with DSPE-mPEG$_{2000}$ via hydrophobic interactions between DSPE and OA to obtain UCNPs-PEG, forming a bilayer structure with a hydrophobic OA/DSPE inner layer and a hydrophilic PEG outer layer (Figure S6A, UCNPs-PEG). The as-obtained UCNPs-PEG demonstrated a hydrate diameter of ~66 nm and zeta potential of ~ −10 mV (Figure S6B,C, UCNPs-PEG). To prepare NIR-DNA shutter UCNPs-$S1_{Azo}/S2_{Azo}$, DNA strands cho-$S1_{Azo}$ and cho-$S2_{Azo}$ were anchored to the OA/DSPE inner layer with cholesterol as a hydrophobic anchor. This is a commonly used surface modification process, which is a thermodynamically favorable process and is quickly completed. While the 15-nt poly-T spacer region propped up the hybridization region of cho-$S1_{Azo}$/cho-$S2_{Azo}$ beyond the PEG outer layer to ensure efficient hybridizations (Scheme 1B, Figure S6A, NIR-DNA shutter). To prevent hybridization of cho-$S1_{Azo}$ and cho-$S2_{Azo}$ during the preparation process, both DNA strands were preirradiated with UV light to turn Azo to *cis*-isomerizatoin that is unfavorable for DNA hybridization before incubating with UCNPs-PEG. The as-obtained NIR-DNA shutter showed an increase of hydrated diameter to ~81 nm and a decrease of zeta potential to ~ −31 mV (Figure S6B,C, NIR-DNA shutter). NIR-DNA shutter also showed an obvious characteristic absorption peak of DNA at 260 nm in the UV−visible absorption spectrum (Figure S6D, NIR-DNA shutter). The anchoring of DNA strands on the UCNPs' surface was further evaluated by fluorescence spectra. FAM dye-labeled cho-$S1_{Azo}$ (cho-$S1_{Azo/FAM}$) and cho-$S2_{Azo}$ (cho-$S2_{Azo/FAM)}$ were incubated with UCNPs-PEG, and the as-obtained NIR-$DNA_{FAM}$ shutter showed strong FAM fluorescence (Figure 2D, NIR-$DNA_{FAM}$ shutter). In comparison, UCNPs-PEG were also incubated with $S1_{Azo/FAM}$ and $S2_{Azo/FAM}$ that in the absence of cholesterol modification, which demonstrated substantially lower fluorescence compared with the NIR-$DNA_{FAM}$ shutter (Figure 2D, +$S1_{Azo/FAM}/S2_{Azo/FAM}$). These results indicated the low degree of nonspecific adsorption from DNA strands cho-$S1_{Azo/FAM}$ and cho-$S2_{Azo/FAM}$ and their anchoring to UCNPs-PEG were predominantly attributed to the hydrophobic−hydrophobic interaction between the cholesterol head of DNA strands and DSPE. The coverage density of DNA strands on UCNPs-PEG was evaluated by comparing the fluorescence intensity of NIR-$DNA_{FAM}$ shutter with the standard calibration curve of cho-$S1_{Azo/FAM}$/cho-$S2_{Azo/FAM}$ (Figure S7), and the number of surface-anchored DNA strands was determined as ~150 per particle. Accordingly, the average distance among DNA strands on the UCNP surface was calculated as ~3.3 nm. Considering

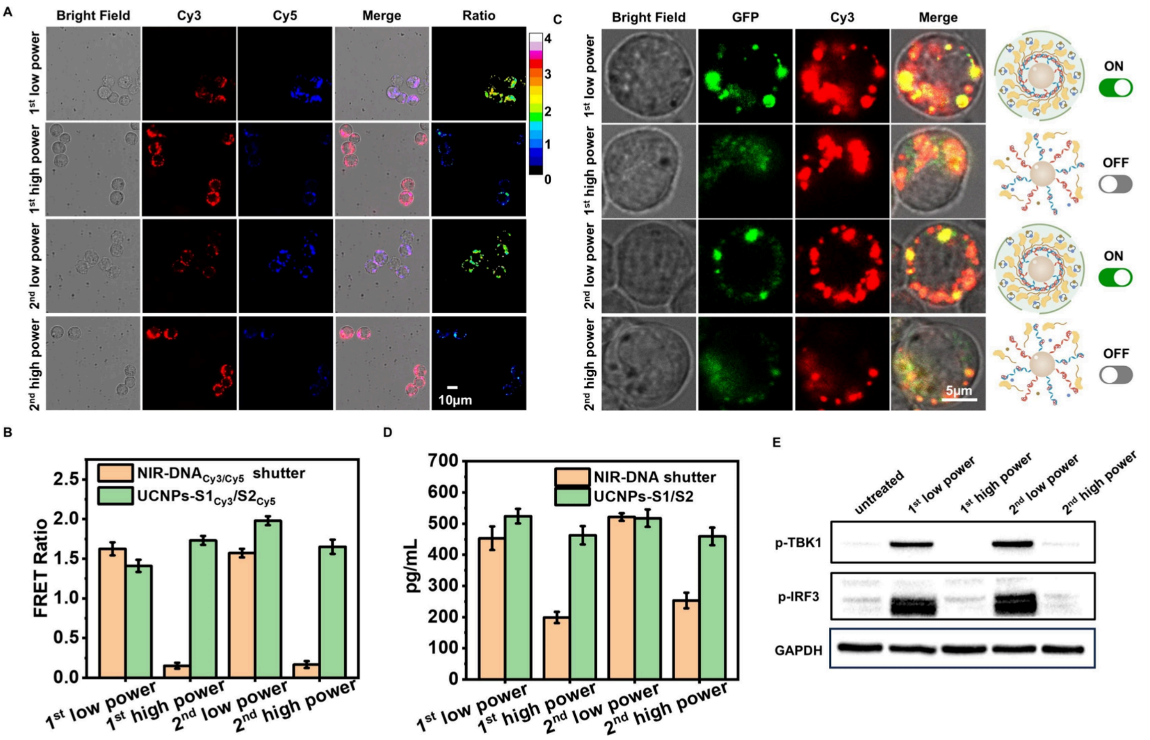

**Figure 3.** NIR light programmed status conversion of NIR-DNA shutter and corresponding "activation-rest" interval of cGAS-STING pathway. (A) Confocal images and (B) corresponding Cy5/Cy3 FRET ratio of Raw264.7 cells treated with NIR-DNA$_{Cy3/Cy5}$ shutter and exposed with 2 cycles of low/high power 808 nm laser irradiations. The Cy5/Cy3 channel imaging ratio obtained from ImageJ processing was represented in a 16-color format. (C) Confocal images of reversible intracellular GFP-cGAS liquid phase condensation and (D) ELISA measurement of IFN-$\beta$ secretion in response to 2 cycles of low/high power 808 nm laser irradiations. (E) Western blot analysis of signaling proteins expressed in the cGAS-STING pathway of Raw264.7 cells treated with NIR-DNA shutter in response to 2 cycles of low/high power 808 nm laser irradiations.

the hybridization region length of ~5.4 nm, the packing density of DNA strands is sufficient for the assembly and disassembly of the dsDNA chain along the UCNPs surface (Figure 2E).

**NIR-Switched Reversible dsDNA Assembly and Disassembly.** NIR programmed isomerization of Azo, that modified in S1$_{Azo}$/S2$_{Azo}$, was verified by UV−Vis spectra. NIR-DNA shutter showed DNA characteristic absorption peak at 260 nm and Azo characteristic absorption peak at 340 and 430 nm (Figure S8). Low power 808 nm light irradiation resulted in an increase for 340 nm absorbance peak that corresponded to $\pi-\pi^*$ transition of *trans*-Azo[41] and a decrease for 430 nm absorbance peak that corresponded to n−$\pi^*$ transition of *cis*-Azo[41] (Figure S8, 1st low power), indicating the corresponding transition of Azo from *cis*-isomerization to *trans*-isomerization. Subsequent high power 808 nm irradiation resulted in an obvious decrease in the *trans*-Azo characteristic absorbance peak at 340 nm and an increase in the *cis*-Azo characteristic absorbance peak at 430 nm (Figure S8, 1st high power), indicating the corresponding transition of Azo from *trans*-isomerization to *cis*-isomerization. Low power and high power 808 nm NIR irradiation were repeated sequentially and demonstrated the same intensity change tendency for both *trans*-Azo and *cis*-Azo characteristic absorbance peaks as in the first cycle (Figure S8, 2nd low power, 2nd high power). These results confirmed the reversible Azo isomerization conversion switched by NIR excitation power density.

To visualize the NIR power density switched status conversion of NIR-DNA shutter via fluorescence spectra, the 3′ terminus and 5′ terminus of DNA strand cho-S1$_{Azo}$ and cho-S2$_{Azo}$ were labeled with Cy3 and Cy5, respectively (S1$_{Azo/Cy3}$, S2$_{Azo/Cy5}$) to prepare NIR-DNA$_{Cy3/Cy5}$ shutter. Low power 808 nm light irradiation (0.75 W/cm$^2$) switched NIR-DNA$_{Cy3/Cy5}$ shutter to "ON" status with *trans*-Azo, and induced alternative hybridization of S1$_{Azo/Cy3}$ and S2$_{Azo/Cy5}$ along the UCNPs surface to form a dsDNA chain (Figure 2F, low power). The formation of the dsDNA chain resulted in proximity of Cy3 and Cy5 and efficient FRET process with a substantial increase of Cy5/Cy3 fluorescence intensity ratio (F670/F570) (Figure 2G, 1st cycle, low power, Figure 2H, NIR-DNA$_{Cy3/Cy5}$ shutter, 1st, low). High power 808 nm light irradiation (2.1 W/cm$^2$) switched NIR-DNA$_{Cy3/Cy5}$ shutter to "OFF" status with *cis*-Azo, which dehybridized the dsDNA chain and significantly decreased F670/F570 by ~85% (Figure 2G, 1st cycle, high power, Figure 2H, NIR-DNA$_{Cy3/Cy5}$ shutter, 1st, high). The alternate low power/high power irradiation cycles were repeated for three cycles and seven cycles and demonstrated similar tendency of F670/F570 ratio changes (Figure 2G, 2nd cycle, 3rd cycle, Figure 2H, NIR-DNA$_{Cy3/Cy5}$ shutter, 2nd, 3rd, Figure S9), indicating good reversibility, durability, and efficiency of NIR-DNA shutter as intermittent STING agonist for manipulating dsDNA chain assembly and disassembly. In comparison, UCNPs-S1$_{Cy3}$/S2$_{Cy5}$, as constant STING agonists, were prepared by conjugating the "unreversible" control group, cho-S1$_{Cy3}$ and cho-S2$_{Cy5}$, which, in the absence of Azo modification, to the UCNP surface (Figure S10A). The constant STING agonist could not make reversible dsDNA chain assembly/disassembly and remained at "ON" status with a high F670/F570 ratio regardless of low power or high power NIR irradiations (Figure 2H, UCNPs-S1$_{Cy3}$/S2$_{Cy5}$, Figure S10B). These results indicated the critical role of the status switchable DNA shutter in the reversibility control of dsDNA chain assembly.

In addition, UCNPs-S1$_{Azo/Cy3}$ that were only functionalized with cho-S1$_{Azo/Cy3}$ and UCNPs-S2$_{Azo/Cy5}$ that were only functionalized with cho-S2$_{Azo/Cy5}$ were mixed, which barely showed a FRET signal corresponding to both low power and high power 808 nm irradiation (Figure S11). These results indicated that interparticle DNA hybridization barely occurred with little particle aggregation.

The activation of cGAS to promote cGAMP production is accompanied by DNA-induced phase separation[42] (Figure 2I); therefore, the feasibility of manipulating cGAS-STING pathway activation and rest was further confirmed by verifying droplet formation and decomposition in vitro. NIR-DNA shutter, as the intermittent STING agonist, was mixed with FITC-labeled cGAS (cGAS$_{FITC}$), which demonstrated FITC fluorescent droplet-like structures with ~5 $\mu$m upon low power 808 nm irradiation (Figure 2J, 1st low power), suggesting the generation of liquid−liquid phase separation due to the efficient binding of cGAS$_{FITC}$ to the NIR-DNA shutter with "ON" status. FITC fluorescent droplet disappeared upon high power 808 nm irradiation, which indicated the release of cGAS$_{FITC}$ from NIR-DNA shutter with "OFF" status (Figures S12A and 2J, 1st high power). Alternate low power and high power NIR irradiation was repeated and demonstrated a similar tendency of FITC droplet formation and decomposition over seven cycles (Figure 2J, 2nd low power, 2nd high power, Figure S13). On the contrary, constant STING agonist UCNPs-S1/S2 was also incubated with cGAS$_{FITC}$, which remained at "ON" status due to the failure to reversibly control dsDNA assembly and showed FITC fluorescent droplet structures regardless of low power or high power 808 nm irradiation (Figure S12B,C).

**Intracellular Characterization of NIR-DNA Shutter As NIR-Programmed Intermittent STING Agonist.** To visualize internalization of intermittent STING agonist, the NIR-DNA$_{Cy3}$ shutter was prepared by conjugating Cy3-labeled strand cho-S1$_{Azo/Cy3}$ and cho-S2$_{Azo/Cy3}$ to UCNPs-PEG and incubated with RAW264.7 cells. Lipofectamine 3000 was employed to transfect the NIR-DNA$_{Cy3}$ shutter into RAW264.7 cells, and confocal microscopy showed strong intracellular Cy3 fluorescence after 8 h of incubation. Lysosomal staining colocalization also demonstrated separation of Lyso-Green fluorescence and Cy3 fluorescence, indicating efficient lysosomal escape of the NIR-DNA$_{Cy3}$ shutter (Figure S14). These results indicated the efficient intracellular delivery of the NIR-DNA$_{Cy3}$ shutter. Internalization of NIR-DNA shutter and subsequent alternative high power/low power NIR irradiation did not affect the viability of RAW264.7 cells and demonstrated over 85% of cell viability in standard 3-(4,5-dimethylthiazol-2-yl)-2-diphenyltetrazolium bromide (MTT) assay (Figure S15).

The feasibility of the NIR-DNA shutter in switching intracellular reversible dsDNA chain assembly/disassembly was evaluated by fluorescence imaging. NIR-DNA$_{Cy3/Cy5}$ shutter was pretreated with high power 808 nm light to make Azo in *cis*-isomerization unfavorable for DNA hybridization and subsequently incubated with RAW264.7 cells. Low power (0.75 W/cm$^2$) 808 nm laser irradiation resulted in strong intracellular Cy5 fluorescence under 540 nm excitation, indicating an efficient FRET process with NIR-DNA$_{Cy3/Cy5}$ shutter at "ON" status (Figure 3A, 1st low power). Subsequent high power (2.10 W/cm$^2$) 808 nm irradiation switched the NIR-DNA$_{Cy3/Cy5}$ shutter to "OFF" status and significantly decreased the intracellular Cy5 FRET signal (Figure 3A, 1st high power). The alternate low power and high power 808 nm irradiation were repeated for 2 cycles and demonstrated a similar tendency of FRET fluorescence signal change (Figure 3A, 2nd low power, 2nd high power).

The FRET ratio of Cy5/Cy3 fluorescence intensity was quantified in response to two cycles of 808 nm NIR irradiation power changes, which demonstrated ratio value ~1.5 in response to low power 808 nm irradiation and ratio value ~0.16 in response to high power 808 nm irradiation (Figure 3B, NIR-DNA$_{Cy3/Cy5}$ shutter), and was visualized in 16-color format image (Figure 3A, Ratio). These results confirmed the good reversibility of NIR-DNA shutter switching in response to NIR irradiation power density. To evaluate the structural integrity of the NIR-DNA$_{Cy3/Cy5}$ shutter during status conversions, RAW264.7 cells were also excited with 540 nm light and 620 nm light after the 2nd high power 808 nm irradiation, which generated Cy3 fluorescence and Cy5 fluorescence, respectively, with the NIR-DNA$_{Cy3/Cy5}$ shutter in "OFF" status. The good overlap of intracellular Cy3 and Cy5 fluorescence indicated good structure integrity of the NIR-DNA$_{Cy3/Cy5}$ shutter during the repetitive 808 nm excitation power switching process (Figure S16). In comparison, RAW264.7 cells were also incubated with a constant STING agonist, UCNPs-S1$_{Cy3}$/S2$_{Cy5}$. Constant STING agonist remained at status "ON" with hybridized dsDNA chain in the absence of Azo modification, and the FRET ratio of Cy5/Cy3 fluorescence could not demonstrate reversible value switch and remained at ~1.8 regardless of 808 nm excitation light power conversion (Figures S17 and 3B, UCNPs-S1$_{Cy3}$/S2$_{Cy5}$).

The binding of cGAS to dsDNA would result in intracellular phase separations.[42] To visualize the intracellular reversible process of cGAS binding to NIR-DNA shutter and release, the plasmid pEGFP-C3-cGAS was transferred into RAW264.7 cells to obtain RAW264.7 cells that expressed GFP-stained cGAS (GFP-RAW264.7). NIR-DNA$_{Cy3}$ shutter was synthesized by conjugating cho-S1$_{Azo/Cy3}$ and cho-S2$_{Azo/Cy3}$ to UCNPs-PEG, and incubated with GFP-RAW264.7 cells. After low power 808 nm light irradiation to switch on the NIR-DNA$_{Cy3}$ shutter, GFP-RAW264.7 cells were continuously incubated for 4 h to evaluate intracellular phase separation. CLSM images showed the formation of GFP-stained droplet-like structures, indicating efficient intracellular liquid−liquid phase separation. The GFP-stained droplet-like structure overlapped well with the Cy3 fluorescence signal from the NIR-DNA$_{Cy3}$ shutter, confirming efficient binding of GFP-cGAS protein to the NIR-DNA shutter when it switched to "ON" status (Figure 3C, 1st low power). Subsequent high power 808 nm light irradiation switched off the NIR-DNA$_{Cy3}$ shutter, and the GFP-cGAS droplet-like structure disappeared after continuous 4 h incubation (Figure 3C, 1st high power), indicating the release of GFP-cGAS from the NIR-DNA shutter when it switched to "OFF" status. The alternate low power and high power 808 nm irradiations were repeated for 2 cycles and demonstrated reversible appearance/disappearance of GFP-cGAS stained droplet-like structure (Figure 3C, 2nd low power, 2nd high power). The reversible generation and decomposition of GFP-cGAS liquid-phase condensation in response to low/high powers 808 nm light irradiation periods guaranteed the capability of NIR-DNA shutter as an intermittent STING

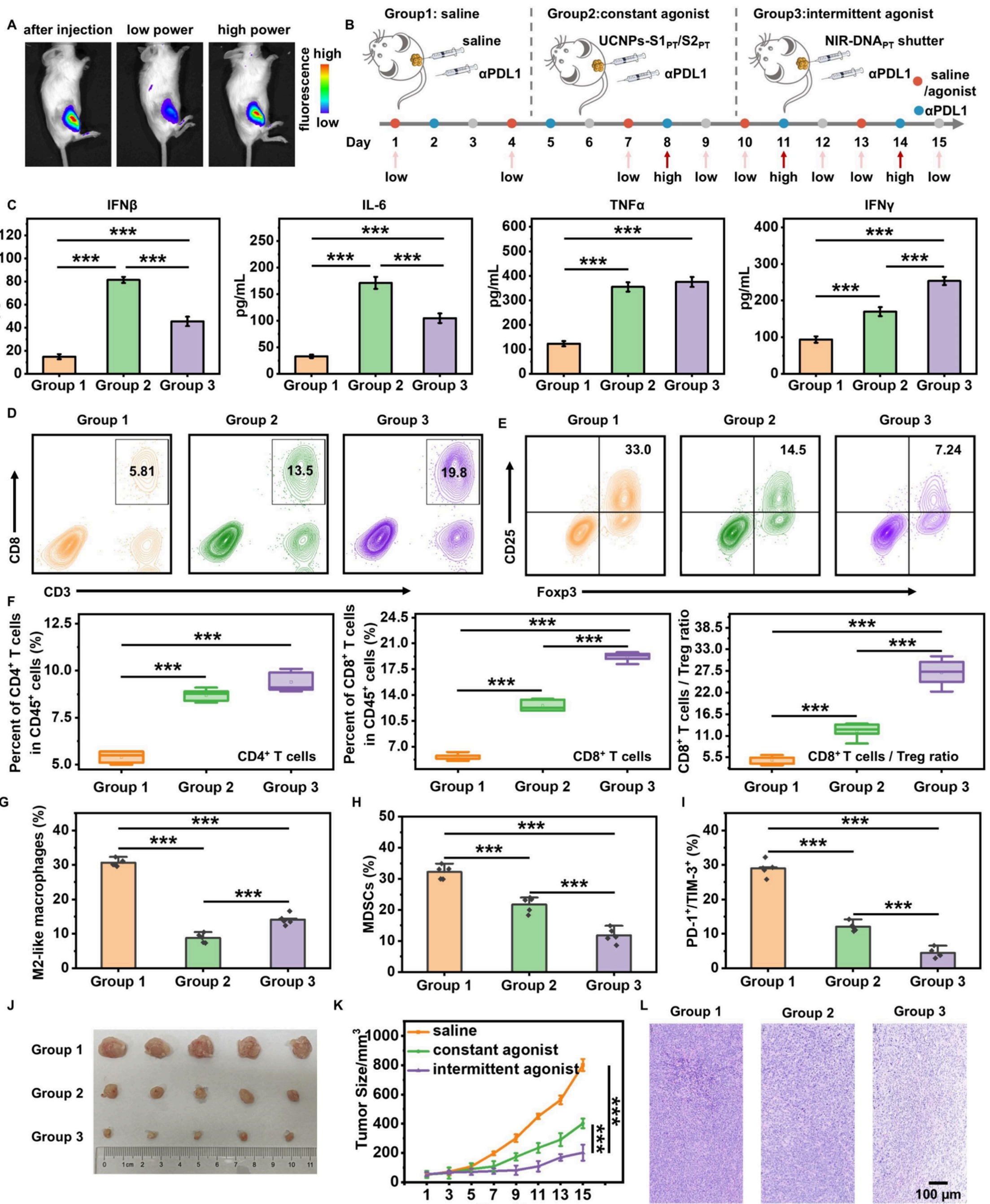

**Figure 4.** Evaluation of antitumor immunotherapy of intermittent STING agonist in vivo. (A) In vivo fluorescence imaging of 4T1-bearing *BALB/c* mice injected with NIR-DNA$_{PT/Cy5/BHQ3}$ shutter under alternate low power and high power 808 nm laser irradiation. (B) Schematic illustration of treatment for subcutaneous 4T1 tumor mice models with group 1: saline, group 2: constant STING agonist UCNPs-S1$_{PT}$/S2$_{PT}$ and group 3: intermittent STING agonist NIR-DNA$_{PT}$ shutter. (C) ELISA detection of IFN$\beta$, IL-6, TNF-$\alpha$ and IFN-$\gamma$ in serum. Representative flow cytometry dot plots of (D) CD8$^+$ T cells and (E) Treg cells. Flow cytometric analysis of immunostimulatory effect in 4T1 tumor-bearing mice, including (F) infiltration of CD4$^+$ T and CD8$^+$ T cells in tumors, ratio of CD8$^+$ T and Treg cells, percentage ratio of (G) M2-like macrophages, (H) MDSCs and (I) exhaustion of CD8$^+$ T cells. (J) Photographs of dissected 4T1 mice tumors, (K) tumor volume change curves, and (L) H&E staining of 4T1 tumors for mice groups treated with group 1: saline, group 2: constant STING agonist, and group 3: intermittent STING agonist, respectively. The error bars in (C) and (K) indicate means ± SD ($n = 5$). Statistical analysis was carried out via one-way analysis of variance (ANOVA) with Tukey's multiple comparison test, * $p \leq 0.05$, ** $p \leq 0.01$, *** $p \leq 0.001$. Gating strategies for (D), (E), (F), and (I) are presented in Figure S30, and those for (G) and (H) are presented in Figure S31.

agonist to regulate cGAS-STING pathway with "activation-rest" intervals.

Cytokine IFN-$\beta$ secretions from RAW264.7 cells, which directly reflect cGAS-STING pathway activation, were measured with enzyme-linked immunosorbent assay (ELISA) to evaluate the "activation-rest" intervals of the cGAS-STING pathway. Compared to untreated RAW264.7 cells, incubation with NIR-DNA shutter alone, only irradiated with alternate low/high 808 nm irradiations, or with alternate high/low 808 nm irradiations could not activate the cGAS-STING pathway, and barely resulted in IFN-$\beta$ secretion (Figure S18). Low power 808 nm irradiation switched on the NIR-DNA shutter and activated the cGAS-STING pathway, which significantly prompts IFN-$\beta$ secretion (Figure 3D, NIR-DNA shutter, 1st low power). On the contrary, high power 808 nm irradiation switched off the NIR-DNA shutter and paused the cGAS-STING pathway, which obviously reduced the IFN-$\beta$ secretion level by 62.5% (Figure 3D, NIR-DNA shutter, 1st high power). The "activation" and "rest" intervals were repeated for 2 cycles by alternate low/high power 808 nm irradiations and correspondingly caused reversible increase and decrease of IFN-$\beta$ secretion levels (Figure 3D, NIR-DNA shutter, 2nd low power, 2nd high power), indicating the capability of NIR-DNA shutter for reversible manipulation of the cGAS-STING pathway. IFN-$\beta$ secretion from RAW 264.7 cells that were treated with a constant STING agonist, UCNPs-S1/S2, was also measured. The constant STING agonist kept the activation of the STING pathway and demonstrated high levels of IFN-$\beta$ secretion regardless of low/high power 808 nm irradiations (Figure 3D, UCNPs-S1/S2).

Phosphorylation of TBK1 and IRF3 serves as an important indicator for evaluating cGAS-STING pathway activation. Therefore, Western blot analysis was performed to characterize the phosphorylation of these two key signaling molecules after 20 h of 808 nm laser irradiation to evaluate cGAS-STING pathway manipulation with "activation-rest" intervals (Figure 3E). Low power 808 nm irradiation switched on the NIR-DNA shutter and activated the cGAS-STING pathway, which significantly improved p-TBK1 and p-IRF3 expression (Figure 3E, 1st low power). Subsequent high power 808 nm irradiation switched off the NIR-DNA shutter and paused the cGAS-STING pathway, which obviously reduced p-TBK1 and p-IRF3 expression (Figure 3E, 1st high power). The "activation" and "rest" intervals were repeated for 2 cycles by alternate low/high power 808 nm irradiations and correspondingly caused reversible increase and decrease of p-TBK1 and p-IRF3 expression levels (Figure 3E, 2nd low power, 2nd high power), indicating the capability of NIR-DNA shutter for reversible manipulation of the cGAS-STING pathway. In comparison, p-TBK1 and p-IRF3 expression of RAW 264.7 cells that were treated with constant STING agonist, UCNPs-S1/S2, were also measured. The constant STING agonist kept the activation of the STING pathway and demonstrated high levels of p-TBK1 and p-IRF3 expression regardless of low/high power 808 nm irradiations (Figure S19).

To rule out the possibility of DNA modification or photoisomerization of Azo to activate the cGAS-STING pathway, the NIR-DNA shutter was pretreated with high power 808 nm light to make the NIR-DNA shutter in "OFF" status, and subsequently incubated with cGAS$_{\mathrm{FITC}}$ and RAW264.7 cells without any further irradiation. Neither liquid−liquid phase separation generation nor increased p-TBK1 and p-IRF3 expression was observed (Figure S20A,B, +NIR-DNA shutter). In addition, UCNPs-S1$_{\mathrm{Azo}}$ with only cho-S1$_{\mathrm{Azo}}$ anchoring was prepared and incubated with cGAS$_{\mathrm{FITC}}$ and RAW264.7 cells in response to high power and low power 808 nm laser irradiation, respectively, which barely demonstrated LLPS condensate generation nor p-TBK1 and p-IRF3 expression increase (Figure S20A,B, +UCNPs-S1$_{\mathrm{Azo}}$ + low power, +UCNPs-S1$_{\mathrm{Azo}}$ + high power). These results indicated that neither DNA modification nor Azo configuration change would affect the cGAS-STING pathway.

**In Vivo Immunotherapy with "Activation-Rest" Intervals via NIR-Programmed Intermittent STING Agonist.** Although the cGAS-STING pathway is one of the most prevalent targets for reshaping the immune microenvironment, it is worth noting that continuous activation of this pathway can lead to immune exhaustion and induce resistance.[14−17] Intermittent activation treatment has been proposed as an effective strategy, where alternating periods of immune activation and cessation allow cells to reverse transcriptional changes associated with resistance, thereby facilitating immune cell recovery and resensitization with enhanced immunotherapy efficiency.[18] To improve in vivo structure stability and prevent nuclease degradation,[43] the NIR-DNA$_{\mathrm{PT}}$ shutter was prepared with phosphorothioate-modified DNA strands, cho-S1$_{\mathrm{Azo/PT}}$ and cho-S2$_{\mathrm{Azo/PT}}$. The serum stability of S1$_{\mathrm{Azo/PT}}$ and S2$_{\mathrm{Azo/PT}}$ was verified by PAGE analysis, which demonstrated stable DNA bands for 72 h of 10% fetal bovine serum (FBS) treatment (Figure S21). To further evaluate the in vivo accumulation and metabolism of the NIR-DNA shutter, the NIR-DNA$_{\mathrm{PT/Cy5}}$ shutter was synthesized with cho-S1$_{\mathrm{Azo/PT/Cy5}}$ and cho-S2$_{\mathrm{Azo/PT/Cy5}}$. The as-obtained NIR-DNA$_{\mathrm{PT/Cy5}}$ shutter was intratumorally injected into 4T1-bearing mice, and strong Cy5 fluorescence was sustained at the tumor position for 72 h (Figure S22), indicating the effective in vivo retaining of intermittent STING agonist.

To visualize the in vivo reversible status switch of NIR-DNA shutter, NIR-DNA$_{\mathrm{PT/Cy5/BHQ3}}$ shutter was synthesized using UCNPs-PEG and cho-S1$_{\mathrm{Azo/PT/Cy5}}$ and cho-S2$_{\mathrm{Azo/PT/BHQ3}}$, which were labeled with Cy5 and BHQ3 at the 3′ terminus of S1$_{\mathrm{Azo/PT}}$ and 5′ terminus of S2$_{\mathrm{Azo/PT}}$, respectively. The as-obtained NIR-DNA$_{\mathrm{PT/Cy5/BHQ3}}$ shutter was preirradiated with high power 808 nm irradiation to switch to "OFF" status, and clearly showed Cy5 fluorescence at the tumor site after administration (Figure 4A, after injection). Low power 808 nm irradiation switched on NIR-DNA$_{\mathrm{PT/Cy5/BHQ3}}$ shutter, and the corresponding hybridization of S1$_{\mathrm{Azo/PT/Cy5}}$ and S2$_{\mathrm{Azo/PT/BHQ3}}$ resulted in proximity of Cy5 and BHQ3 with significant quenching of Cy5 fluorescence at the tumor site (Figure 4A, low power). Subsequent high power 808 nm irradiation switched off the NIR-DNA$_{\mathrm{PT/Cy5/BHQ3}}$ shutter and resulted in an efficient recovery of Cy5 fluorescence at the tumor position with comparable intensity to the original level just after administration (Figure 4A, high power). These results confirmed the efficient in vivo status "ON/OFF" switch of the NIR-DNA$_{\mathrm{PT/Cy5/BHQ3}}$ shutter in response to low/high power 808 nm irradiations.

Considering cGAS-STING agonists, which act as a link between innate and adaptive immunity, are usually combined with ICB therapy to enhance therapeutic effect; therefore, intermittent STING agonist NIR-DNA shutter was combined with ICB reagent anti-PDL1 antibody ($\alpha$PDL1) to verify the in vivo therapeutic effect. 4T1 tumor-bearing *BALB/c* mice were randomly divided into three groups when the tumor size grew to around 60 mm$^3$, and administered with saline, intermittent STING agonist NIR-DNA$_{\mathrm{PT}}$ shutter, and constant STING agonist UCNPs-S1$_{\mathrm{PT}}$/S2$_{\mathrm{PT}}$, respectively, every 3 days. All mice were injected with $\alpha$PD-L1 intraperitoneally on the day after agonist administration. Both the intermittent STING agonist treatment group and constant STING agonist treatment group were irradiated with a low power 808 nm laser only on the day of agonist administration for the first 6 days and were irradiated with alternate low power or high power 808 nm laser every 24 h after each time agonist administration for the rest of treatment period (Figure 4B). ELISA assays were performed to investigate proinflammatory cytokines secretion in serum after 15 days of treatment. Compared with the saline-administered mice group, both constant STING agonist UCNPs-S$1_{PT}$/S$2_{PT}$ and intermittent STING agonist NIR-$DNA_{PT}$ shutter administrated group demonstrated obvious enhancement for cytokine secretion levels of IFN-$\beta$, IFN-$\gamma$, TNF-$\alpha$, and IL-6 (Figure 4C). IFN-$\beta$ and IL-6 were determined as the indicators for STING activation; thus, higher secretion levels were observed from the constant STING agonist-administered group compared with the intermittent STING agonist-administered group (Figure 4C, IFN$\beta$, IL-6). TNF-$\alpha$ secretion was stimulated by both STING activation and T cell activation, thus demonstrating a similar level from both the constant STING agonist-administered group and the intermittent STING agonist-administered group (Figure 4C, TNF$\alpha$). IFN$\gamma$ secretion was attributed to T cell activation but not STING activation; therefore, the intermittent STING agonist-administered group showed a higher level compared with the constant STING agonist-administered group (Figure 4C, IFN$\gamma$), indicating that the intermittent STING activation mode benefited T cell activation. To further compare the effects of intermittent STING agonist and constant STING agonist on T cell activation, the tumors were collected from three groups after treatment for immunoassays. Flow cytometry analysis revealed an obvious increase in the infiltration of $CD4^+$ T cells and $CD8^+$ T cells in tumors for both the intermittent agonist-administered group and the constant agonist-administered group compared with the saline-administered group (Figure 4D, F). The proportion of $CD4^+$ T cells in $CD45^+$ cells increased from ~5.43% for the saline-treated group to ~8.70% for the constant STING agonist-treated group and ~9.42% for the intermittent agonist-treated group (Figure 4F, $CD4^+$ T cells, Figure S23). The proportion of $CD8^+$ T cells in $CD45^+$ cells increased from ~5.61% for the saline-treated group to ~ 12.61% for the constant STING agonist-treated group and ~19.18% for the intermittent agonist-treated group (Figure 4D,F, $CD8^+$ T cells). The ratio of cytotoxic T cells to regulatory T cells was also evaluated, which was ~4.83 for the saline-treated group, ~12.21 for the constant-agonist-treated group, and ~27.06 for the intermittent-agonist-treated group (Figure 4E,F, $CD8^+$ T cells/Treg ratio). To further explore the enhanced efficiency of intermittent STING agonist over constant STING agonist, flow cytometry analysis was performed to quantify the proportions of M2-like macrophages, myeloid-derived suppressor cells (MDSCs), and exhausted T cells within the tumor microenvironment (Figures 4G−I and S24). The proportion of M2-like macrophages decreased from ~30.64% for the saline-treated group to ~9.89% for the constant STING agonist-treated group due to STING pathway activation **directly** facilitating repolarization of M2-like macrophages toward an M1-like phenotype,[44,45] and ~14.12% for the intermittent agonist-treated group (Figures 4G and S24A). The proportion of MDSCs decreased from ~32.22% for the saline-treated group to ~22.38% for the constant STING agonist-treated group and ~11.78% for the intermittent agonist-treated group (Figures 4H and S24B). The proportion of exhausted T cells decreased from ~28.98% for the saline-treated group to ~12.06% for the constant STING agonist-treated group and ~5.43% for the intermittent agonist-treated group (Figures 4I and S24C). These results indicated that intermittent activation has superior efficacy and stronger potential in regulating the immunosuppressive microenvironment, which resulted in enhanced antitumor immunity.

The tumor volume and body weight of mice from 3 groups were measured every 2 days to evaluate antitumor efficacy. The saline-administered group exhibited rapid tumor growth, and both STING agonist-treated groups showed effective suppression of tumor growth. The constant STING agonist-treated group and intermittent STING agonist-treated group did not demonstrate obvious tumor size difference during the first 7 days of treatment since only low power 808 nm irradiations were performed during this period. After 15 days of treatment, the intermittent STING agonist-treated group showed superior tumor growth inhibition with ~70% reduction in tumor size, and the constant STING agonist-treated group showed ~35% reduction in tumor size (Figure 4J,K). In addition, H&E and TUNEL-stained images of mouse tumor slices demonstrated a similar tendency with the most significant cell nuclei shrinkage and visible apoptosis of tumor cells for intermittent STING agonist-treated mice group (Figures 4L and S25). All mouse groups did not show a significant change in body weight (Figure S26) and obvious pathological abnormalities of major organs during the experimental period (Figure S27), confirming the excellent biosafety of the NIR-DNA shutter and irradiation.

The therapeutic effects for different light power switching internals of intermittent STING agonist were further explored (Figure S28). 24h alternating irradiation regimen from the first day exhibited compromised therapeutic outcomes due to insufficient immune activation (Figure S28, Group 1). A shorter interval regimen was set by irradiating the tumor with a low power 808 nm laser for the first 6 days, followed by a 6 h alternating power switching pattern for the rest of the treatment period, which also showed diminished therapeutic efficacy (Figure S28, Group 2) compared to the 24 h alternating activation group (Figure S28, Group 3). This may be due to the inefficient clearing of STING signaling with a shortened termination period.

## ■ CONCLUSIONS

In summary, we developed a NIR-DNA shutter here as an intermittent STING agonist to stimulate the STING pathway in a repetitive “activation-rest” interval for enhancing immunotherapy efficiency. The NIR-DNA shutter was constructed by conjugating Azo-modified complementary DNA strands to the UCNPs. Reversible assembly and disassembly of dsDNA along the UCNPs surface were manipulated by alternate low power and high power 808 nm NIR irradiations, which induced *trans*- and *cis*-isomerization of Azo, respectively. By switching the excitation power of 808 nm light, the NIR-DNA shutter was reversibly converted between “ON/OFF” states, therefore, programmed the cGAS-STING pathway with “activation-rest” intervals. This strategy remodeled the immunosuppressive tumor microenvironment by reducing the suppressive activity of regulatory T cells (Tregs) and enhancing dendritic cell-mediated cross-priming of $CD8^+$ cytotoxic T cells. Compared with constant STING activation that may induce T cell exhaustion, this approach achieved superior antitumor efficacy.

## ■ EXPERIMENTAL SECTION

**Materials.** The high-purity anhydrous rare-earth chloride reagents used in this research were obtained from Sigma-Aldrich (USA), including thulium chloride ($TmCl_3$) (99.9%), ytterbium chloride ($YbCl_3$) (99.9%), yttrium chloride ($YCl_3$) (99.9%), and neodymium chloride ($NdCl_3$) (99.9%). Oleic acid (OA), 1-octadecene (ODE), sodium hydroxide (NaOH), ammonium fluoride ($NH_4F$), dichloromethane (DCM), and chloroform were purchased from Aladin Ltd. (Shanghai, China). DSPE-mPEG$_{2000}$ was purchased from ToYong Biotech (Shanghai, China). Rabbit monoclonal antiphospho-IRF3 (Ser396) (D6O1M) and rabbit monoclonal antiphospho-TBK1/NAK (Ser172) (D52C2) were purchased from Cell Signaling Technology, Inc. (USA). TAK243 was purchased from MedChemExpress, Inc. The protein extraction kit and Lyso-Tracker dye were obtained from Beyotime Biotechnology (Shanghai, China). Enzyme-linked immunosorbent assay (ELISA) was purchased from Elabscience Biotechnology Co., Ltd. (Wuhan, China). 3-(4,5-Dimethylthiazol-2-yl)-2,5-diphenyltetrazolium Bromide Cell Proliferation and Cytotoxicity Assay Kit (MTT) and 2-[4-(2-hydroxyethyl)-1-piperazinyl] ethanesulfonic acid solution (HEPES) were purchased from Keygen Biotech (Nanjing, China). All DNAs were synthesized and purified by Sangon Biotech (Shanghai, China). The sequences for all DNA strands are listed in Table S1.

**Apparatus.** The concentrations of nucleic acids were measured by a NanoDrop 2000 UV−vis spectrophotometer. **Polyacrylamide gel electrophoresis analysis** was conducted using a PowerPac basic electrophoresis analyzer (Bio-Rad, USA). Atomic force microscopy (AFM) imaging under ambient conditions employed tapping mode with a Bruker Dimension Icon microscope. Fluorescence spectral characterization utilized a FluoroMax-4 spectrophotometer (HORIBA Scientific, Japan). Flow cytometry analysis was performed on a CytoFlex S instrument (Beckman-Coulter, USA). Confocal microscopy images were acquired by using a Leica SP8 STED 3X system (Germany). In vivo and ex vivo imaging of mice and harvested organs was carried out on an IVIS Lumina XR III platform (PerkinElmer, USA).

**Synthesis of Core−Shell Upconversion Nanoparticles (UCNPs) $NaYF_4$:Tm,Yb,@$NaYF_4$:Nd,Yb.** Synthesis of UCNPs core $NaYF_4$:0.5%$Tm^{3+}$,30%$Yb^{3+}$: 0.695 mmol of $YCl_3$, 0.300 mmol of $YbCl_3$, and 0.005 mmol of $TmCl_3$ were mixed with 6 mL of oleic acid and 15 mL of 1-octadecene, heated to 150 °C under vacuum, and stirred for 40 min to remove residual water and oxygen completely. After the mixture cooled to room temperature, 10 mL of a methanol solution containing 148 mg of $NH_4F$ and 100 mg of NaOH was added dropwise to the mixture under stirring over 30 min. Next, the reaction mixture was heated under a nitrogen atmosphere, first at 110 °C for 15 min and then at 300 °C for 90 min. Subsequently, the mixture was cooled naturally to room temperature. The as-obtained UCNPs core $NaYF_4$:$Tm^{3+}$, $Yb^{3+}$ was precipitated with acetone, washed repeatedly with ethanol, and redispersed in 10 mL of cyclohexane for later use.

Preparation of shell precursor $NaYF_4$:10%$Nd^{3+}$,10%$Yb^{3+}$: 0.800 mmol of $YCl_3$, 0.100 mmol of $YbCl_3$, and 0.100 mmol of $NdCl_3$ were mixed with 6 mL of oleic acid and 15 mL of 1-octadecene, heated to 150 °C under vacuum, and stirred for 40 min to form a transparent solution, which was then cooled to 40 °C. Then, 10 mL of methanol solution containing 100 mg of NaOH and 148 mg of $NH_4F$ was added and stirred for 0.5 h. The reaction mixture was then heated to 110 °C for 15 min to completely remove methanol and obtain the shell precursor $NaYF_4$:$Nd^{3+}$, $Yb^{3+}$.

Synthesis of core−shell UCNPs $NaYF_4$:0.5%$Tm^{3+}$,30%$Yb^{3+}$@$NaYF_4$:10%$Nd^{3+}$,10%$Yb^{3+}$: Core−shell UCNPs were prepared by using a one-pot successive layer-by-layer (SLBL) method. Added 10 mL of the above-obtained UCNPs core $NaYF_4$: Tm, Yb to 3.0 mL of oleic acid and 9.0 mL of 1-octadecene. The mixture was heated to 85 °C and kept for 30 min to remove cyclohexane, further heated to 300 °C under a nitrogen flow, and injected with the above-obtained precursor $NaYF_4$: $Nd^{3+}$, $Yb^{3+}$, and continuously kept at 300 °C for 30 min to facilitate shell growth. This shell coating process was repeated three times to achieve the desired shell thickness. The as-obtained core−shell UCNPs $NaYF_4$,Tm,Yb @$NaYF_4$,Nd,Yb were precipitated, washed with acetone and ethanol, and redispersed in cyclohexane for further use.

**Photomodulated DNA Assembly/Disassembly.** Photomodulated DNA strand assembly and disassembly were verified via FRET. S1$_{Azo}$ strand was modified with FAM at 3′ terminus (S1$_{Azo/FAM}$), and S2$_{Azo}$ was modified with TAMRA at 5′terminus (S2$_{Azo/TAMRA}$). FAM and TAMRA were placed in proximity to make a FRET signal when S1$_{Azo/FAM}$ and S2$_{Azo/TAMRA}$ were assembled.

S1$_{Azo/FAM}$ and S2$_{Azo/TAMRA}$ were preirradiated by UV light to make azobenzene in *cis*-isomerization, which was not favorable for DNA hybridization. Ten $\mu$M of both DNA strands were mixed in PBS and incubated at 37 °C for 30 min. For photoactivated DNA assembly, the reaction solution was irradiated with 450 nm of Vis light (14 mW/cm$^2$) for 5 min and then incubated at 37 °C for 30 min. For phototriggered disassembly, the above-treated solution was irradiated with 365 nm UV light (6 mW/cm$^2$) for 5 min and then incubated at 37 °C for 30 min. In this way, cyclic irradiation treatment was performed, and the fluorescence intensities of FAM and TAMRA were detected at 500−620 nm under 488 nm excitation, where 500−540 nm was the emission spectrum of FAM, and 565−620 nm was the emission spectrum of TAMRA.

**Gel Electrophoresis Analysis.** Ten microliters of S1 and S2 (10 $\mu$L) were mixed and incubated in PBS (10 mM, 5 mM $MgCl_2$, and 50 mM NaCl) at 37 °C for 30 min for DNA assemblies. The as-obtained products were verified through polyacrylamide gel electrophoresis. 8% native polyacrylamide gel was prepared using 1× TBE buffer. The samples were prepared by mixing 5 $\mu$L of DNA strands with 1 $\mu$L of 6× loading buffer. Polyacrylamide gel electrophoresis was run at 110 V for 50 min in 1× TBE buffer. The gels were stained with SYBR Gold nucleic acid gel stain (Thermo Fisher Scientific, USA), and scanned with a Molecular Imager Gel Doc XR.

**Synthesis of the NIR-DNA Shutter (UCNPs-S1$_{Azo}$/S2$_{Azo}$) as an Intermittent Agonist.** Twenty-five mg of the above-obtained UCNPs were dissolved in 5 mL of chloroform and mixed with 3 mL of chloroform solution containing 25 mg of DSPE-mPEG2000 in a round-bottom flask. The chloroform was then removed by rotary evaporation, and the resulting mixed film was then hydrated with 2-[4-(2-hydroxyethyl)-1-piperazinyl] ethanesulfonic acid solution (HEPES, pH ∼ 7.0, 10 mM, 5 mL) and vigorously sonicated to fully disperse UCNPs in aqueous solution. The as-obtained aqueous phase dispersible UCNPs were purified by centrifugation three times at 18000 rpm for 30 min to remove excess DSPE-mPEG2000 and filtered with a 0.22 $\mu$m filter to remove possible large aggregates to obtain UCNPs-PEG.

Cho-S1$_{Azo}$ and cho-S2$_{Azo}$ were then anchored to the UCNPs-PEG surface via hydrophobic interaction between cholesterol and DSPE to prepare the NIR-DNA shutter (UCNPs-S1$_{azo}$/S2$_{azo}$) as an intermittent agonist. 0.2 mg of the above-obtained UCNPs-PEG was mixed with cho-S1$_{azo}$ (10 $\mu$L, 10 $\mu$M) and cho-S2$_{azo}$ (10 $\mu$L, 10 $\mu$M), and stirred at room temperature for 10 min. Both DNA strands were preirradiated with UV light before incubating with UCNPs, which caused azobenzene to *cis* -isomerization that is unfavorable for DNA hybridization. The resulting NIR-DNA shutters were centrifuged, repeatedly washed with HEPES buffer (pH 7.4, containing 500 mM NaCl), and dispersed in 1 mL of HEPES buffer.

**NIR-Modulated Status Switch of the NIR-DNA Shutter.** NIR-modulated status switch of the NIR-DNA shutter was evaluated by FRET. The Cho-S1$_{Azo}$ strand was modified with Cy3 at 3′ terminus (cho-S1$_{Azo/Cy3}$), and cho-S2$_{Azo}$ was modified with Cy5 at 5′ terminus (cho-S2$_{Azo/Cy5}$). Cy3 and Cy5 were placed in proximity to make a FRET signal when the as-obtained NIR-DNA shutter$_{Cy3/Cy5}$ (UCNPs-S1$_{azo/Cy3}$/S2$_{azo/Cy5}$) was switched on with S1$_{Azo/Cy3}$ and S2$_{Azo/Cy5}$ hybridized to the dsDNA chain.

One mg/mL of NIR-DNA shutter$_{Cy3/Cy5}$ was dispersed in HEPES, pretreated with high power 808 nm light to make Azo in cis-isomerization that unfavorable for DNA hybridization, and then irradiated with a low power 808 nm laser (0.75 W cm$^{-2}$) for 20 min and then incubated at 37 °C for 30 min for dsDNA chain assembly on UCNPs surface to switch NIR-DNA shutter$_{Cy3/Cy5}$ to "ON" status. The as-treated NIR-DNA shutter$_{Cy3/Cy5}$ was subsequently irradiated with a high power 808 nm laser (2.1 W cm$^{-2}$) for 10 min and incubated again at 37 °C for 30 min to switch NIR-DNA shutter$_{Cy3/Cy5}$ to "OFF" status. This cyclical irradiation and incubation procedure was repeated. After each irradiation and incubation, the Cy3 and Cy5 fluorescence intensities were measured at 570 and 670 nm under 540 nm excitation, where 570 nm corresponds to the emission spectrum of Cy3 and 670 nm to the emission spectrum of Cy5.

**AFM Imaging.** A 10-microliter solution of diluted assembled products dsDNA strand was adsorbed onto a freshly cleaved mica surface for 5 min, then rinsed 10 times with deionized water and dried using a nitrogen flow. The samples were scanned in ScanAsyst Mode with ScanAsyst-Air tips, which had a spring constant of 0.4 N/m, a resolution of 256 pixels per line, and a scan rate of 2 Hz. The images were captured and analyzed by using Bruker NanoScope Analysis 1.7 software.

**Dissociation Constant Evaluation.** The FAM-labeled S1$_{Azo/FAM}$ was dissolved in Tris-HCl buffer (10 mM, 50 mM NaCl, and 1 mM $MgCl_2$, pH 7.4), with its final concentration fixed at 0.5 μM. The TAMRA-labeled S2$_{Azo/TAMRA}$ was serially diluted in a concentration gradient ranging from 0.01 nM to 0.5 μM. For the visible light-irradiated group, after being irradiated with 450 nm Vis light (14 mW/cm$^2$) for 5 min, the S1$_{Azo/FAM}$ solution was mixed with gradient concentrations of S2$_{Azo/TAMRA}$ and incubated at 37 °C for 60 min to ensure the binding reaction reached thermodynamic equilibrium. A spectrofluorometer was employed with an excitation wavelength of 488 nm and an emission wavelength scanning range of 500−620 nm, with the fluorescence intensity peak of TAMRA recorded at 580 nm. The fluorescence signal at 0.5 μM S2$_{Azo/TAMRA}$ (saturation concentration) was defined as the 100% bound state, while the signal at 0 nM S2$_{Azo/TAMRA}$ was set as the 0% bound state. Normalized fluorescence signals at intermediate concentrations were calculated accordingly. Data were fitted to a single-site binding model using nonlinear regression analysis: $F = [S2_{Azo/TAMRA}]/(K_d + [S2_{Azo/TAMRA}])$, where $[S2_{Azo/TAMRA}]$ represents the concentration of S2$_{Azo/TAMRA}$. The UV-irradiated group was processed by following the same procedures.

**Surface Coverage Density of S1$_{Azo}$/S2$_{Azo}$ on UCNPs.** To verify the successful modification of S1$_{Azo}$/S2$_{Azo}$ to UCNPs-PEG, fluorescent dye FAM labeled cho-S1$_{Azo}$ (cho-S1$_{Azo/FAM}$) and cho-S2$_{Azo}$(cho-S2$_{Azo/FAM}$) were reacted with UCNPs-PEG according to the above-mentioned procedure. By measuring the FAM characteristic emission at 520 nm for the as-obtained UCNPs-S1$_{Azo/FAM}$/S2$_{Azo/FAM}$ and comparing it with the DNA-FAM calibration curve, respectively, the number of DNA strands per UCNP was quantified.

**In Vitro Phase Separation Assay.** The NIR-DNA shutter (UCNPs-S1$_{azo}$/S2$_{azo}$) (1 mg/mL) was incubated with 0.1 μM FITC-labeled cGAS protein in Tris-HCl buffer (20 mM, pH 7.5, 300 mM NaCl, 20 μM $Zn(CH_3COO)_2$, 1 mg/mL BSA) at 37 °C. The mixtures were irradiated with 808 nm lasers of varying powers for different durations, incubated in test tubes, and then imaged using a Leica TCS SP8 inverted confocal microscope (Leica, Germany).

**Cell Culturing.** RAW264.7 mouse mononuclear macrophages were cultured in high-glucose DMEM medium with 10% FBS, 100 μg/mL penicillin, and 100 μg/mL streptomycin under 5% $CO_2$ at 37 °C. Breast cancer 4T1 cells were cultured under the same conditions, with the exception that RPMI-1640 medium was utilized instead of DMEM.

**Cellular Uptake Analysis.** The RAW264.7 cells were seeded in confocal dishes and cultured overnight, allowing them to reach 80−90% confluence. Following this, the cells were transfected with Cy3-labeled NIR-DNA$_{Cy3}$ shutter in Opti-MEM medium, and incubated at 37 °C. After an 8-h incubation period, the cells were rinsed with PBS. Cellular uptake was then assessed using confocal laser scanning microscopy. LysoTracker Green was used for lysosome staining.

**NIR-Modulated Intracellular Reversible Status Switch of NIR-DNA Shutter.** RAW264.7 cells were incubated with NIR-DNA shutter$_{Cy3/Cy5}$ for 8 h at 37 °C. To switch NIR-DNA shutter$_{Cy3/Cy5}$ to "ON" status, the cells were irradiated with low power 808 nm light (0.75 W/cm$^2$) for 20 min and then incubated for 30 min. To switch NIR-DNA shutter$_{Cy3/Cy5}$ to "OFF" status, the above-treated cells were irradiated with high power 808 nm light (2.1W/cm$^2$) for 10 min and then incubated for 30 min. Cyclic irradiation treatments were performed in this manner. The as-treated cells were analyzed by confocal imaging.

**Intracellular Liquid Phase Condensation Imaging.** RAW264.7 cells (3 × 10$^4$) were seeded into a 4-chamber 35 mm glass-bottom dish and incubated overnight. For transfection, 1 μg of pEGFP-C3-cGAS plasmid was mixed with Lipofectamine 3000 transfection reagent in Opti-MEM, and the mixture was applied to the cells at 37 °C. After 7 h, the transfection solution was removed, and the cells were washed three times with PBS. The culture medium was replaced with DMEM (containing 10% FBS) for an additional 20 h of incubation. Next, 200 μg/mL of NIR-DNA shutter$_{Cy5}$ was added to the medium. Following an 8 h incubation, the cells were exposed to a low power 808 nm laser (0.75 W/cm$^2$) for 20 min and incubated at 37 °C for 4 h. Subsequently, the cells were irradiated with a high power 808 nm laser (2.1W/cm$^2$) for 10 min and incubated at 37 °C for another 4 h. The treated cells were then analyzed using a confocal microscope.

**Cell Viability Assay.** The viability of RAW264.7 cells with different treatments was evaluated through an MTT assay. Briefly, at 24h post NIR-DNA shutter incubation and light irradiation, the culture medium was supplemented with 0.5 mg/mL MTT solution. After another culture at 37 °C for 4 h and the supernatant was carefully removed, followed by the addition of DMSO to dissolve the formazan crystals, and the absorbance at 490 nm was measured. Data was processed according to the manufacturer's instructions and further normalized to the control group.

**Cytokine Evaluation.** After incubating RAW264.7 cells with NIR-DNA shutter for 8 h, they were alternatively exposed to low power 808 nm laser (0.75 W/cm$^2$) and high power 808 nm laser (2.1W/cm$^2$), and continuously incubated for another 20 h after each time light exposure. The culture medium of RAW264.7 cells was then collected and centrifuged at 14,000 g for 10 min at 4 °C. Levels of IFN-β in the supernatants were measured by mouse IFN-β ELISA Kit according to the manufacturer's instructions.

**Western Blot Analysis.** Western blot analysis was used to detect the phosphorylation of IRF3 and TBK1. RAW264.7 cells, after being treated with NIR-DNA shutter and exposed to low power 808 nm laser (0.75 W/cm$^2$) and high power 808 nm laser (2.1W/cm$^2$), respectively, were harvested and lysed on ice using RIPA buffer at 20 h postirradiation, which was supplemented with a cocktail of protease and phosphatase inhibitors. The time interval between the first and second irradiation was 20 h. The samples, after being lysed with RIPA buffer, were centrifuged at 14,000 g for 10 min at 4 °C. The resulting supernatants were mixed with loading buffer and then heated at 95 °C for 10 min to denature the proteins. Subsequently, the denatured samples were loaded onto 12% SDS-PAGE gels for separation, and the proteins were transferred onto PVDF membranes for further analysis. Membranes were first blocked with 5% BSA in Tris-buffered saline containing 0.1% Tween 20 (TBST) for 1 h at room temperature. Following this, the membranes were incubated overnight at 4 °C with the specific primary antibodies: rabbit monoclonal antiphospho-IRF3 (Ser396) (D6O1M), rabbit monoclonal antiphospho-TBK1/NAK (Ser172) (D52C2), and rabbit polyclonal anti-GAPDH, all in TBST. The membranes were washed multiple times with TBST and then incubated with a goat antirabbit HRP-conjugated secondary antibody for 1 h at room temperature. After several additional washes with TBST, the membranes were developed and visualized using a ChemiDoc XRS+ imaging system (BioRad).

**In Vivo Antitumor Evaluation.** All animal experiments were carried out in accordance with the NIH guidelines for the care and use of laboratory animals (NIH Publication No. 85−23 Rev. 1985) and received approval from the Jiangsu Administration of Experimental Animals, under approval number IACUC-2408002.

Phosphorothioate-modified DNA strands S1$_{Azo/PT}$ and S2$_{Azo/PT}$ were used for in vivo experiments to guarantee the in vivo stability of DNA strands. 4T1 cells (2 × 10$^6$ each) were subcutaneously injected into *BALB/c* mice. Once the average tumor volume grown to around 60 mm$^3$, the tumor-bearing mice were divided into three groups, intratumorally injected with 200 μL of (1) saline, (2) constant

STING agonist UCNPs-S$1_{PT}$/S$2_{PT}$ (2 mg/mL), (3) intermittent STING agonist NIR-DNA$_{PT}$ shutter (UCNPs-S$1_{Azo/PT}$/S$2_{Azo/PT}$) (2 mg/mL), followed by intraperitoneal injection of anti-PDL1 antibody ($\alpha$PDL1) for all groups on the next day. Agonists were administered to groups (2) and (3) on the first, fourth, seventh, 10th, and 13th day of treatment. After the first day and fourth day administrations, groups (2) and (3) mice were irradiated with a low power 808 nm laser (0.75 W/cm$^2$) for 20 min. After seventh, 10th, 13th day of treatments, group (2) and (3) mice were treated with 20 min of low power 808 nm laser (0.75 W/cm$^2$) irradiation, followed by 10 min of high power 808 nm laser (2.1 W/cm$^2$) irradiation after 24 h and 20 min of low power 808 nm laser (0.75 W/cm$^2$) irradiation again after 48 h. The body weight and tumor size of the mice were assessed bidaily. Tumor volume was determined using the following formula: Volume = width$^2$ × length × 1/2. After 15 days of treatments, the mice were euthanized, and their organs (heart, liver, spleen, lungs, and kidneys), along with the tumors, were harvested and fixed in 4% PFA. For histological analysis, the organs and tumors were embedded in paraffin and subjected to H&E staining, followed by visualization under a microscope.

**NIR-Modulated Reversible In Vivo Status Switch of the NIR-DNA Shutter.** Cho-S$1_{Azo/PT}$ strand was modified with Cy5 at 3′ terminus (S$1_{Azo/PT/Cy5}$), and the cho-S$2_{Azo/PT}$ strand was modified with BHQ3 at 5′ terminus (S$2_{Azo/PT/BHQ3}$). NIR-DNA$_{PT/Cy5/BHQ3}$ shutter (UCNP-S$1_{Azo/PT/Cy5}$/S$2_{Azo/PT/BHQ3}$) was prepared with cho-S$1_{Azo/PT/Cy5}$ and cho-S$2_{Azo/PT/BHQ3.}$ Cy5 and BHQ3 were placed in proximity to quench Cy5 fluorescence upon dsDNA assembly and recover Cy5 fluorescently upon dsDNA disassembly. Following intratumoral administration of NIR-DNA$_{PT/Cy5/BHQ3}$ shutter, sequential laser irradiation protocols were implemented: a low power 808 nm laser was first applied, followed by a high power 808 nm laser after a 2-h interval. In vivo fluorescence imaging was performed at 1 h postinjection and subsequently after each irradiation session using the IVIS Lumina XR III in vivo imaging system (PerkinElmer, USA).

**Tumor Immune Microenvironment Evaluation.** For immune cell activity assessment in the local tumor environment, mice were euthanized after different treatments to collect blood and tumor tissue. IFN-$\beta$, IFN-$\gamma$, IL-6, and TNF-$\alpha$ levels in mouse serum were measured by ELISA kits.

For flow cytometry analysis, tumors were dissected, minced, and digested with the dissociation buffer containing 1 mg/mL Collagenase I, 0.5 mg/mL DNase I, and 0.5 mg/mL Hyaluronidase at 37 °C for 40 min. Then, the suspension was filtered, centrifuged, and treated with red blood cell lysis buffer. Subsequently, the single-cell suspensions were stained with Fixable Viability Stain 450 and blocked with $\alpha$-CD16/32 for 15 min on ice. The cells were then stained with fluorescent-labeled antibodies including CD45-FITC, CD3-PerCP/Cy5.5, CD4-Alexa Fluor 700, CD8-PE/Cy7, CD25-APC, CD11b-Alexa Fluor 700, Gr-1-PE, F4/80-PE, and CD206-APC. For Foxp3 staining, cells were processed using the eBioscience Foxp3 staining buffer set (Thermo Fisher, 00−5523−00) according to the manufacturer's instructions, followed by staining with Foxp3-PE antibody (Thermo Fisher, 12-4771-82, 1:100). Different cell population was defined as CD8$^+$ T cells: CD45$^+$ CD3$^+$ CD8$^+$; CD4$^+$ T cells: CD45$^+$ CD3$^+$ CD4$^+$; Treg: CD45$^+$ CD3$^+$ CD4$^+$ CD25$^+$ Foxp3$^+$; exhausted T cells: CD45$^+$ CD3$^+$ CD8$^+$ PD-1$^+$ TIM-3$^+$; M2-like macrophages: CD45$^+$ CD11b$^+$ F4/80$^+$ CD206$^+$; MDSCs: CD45$^+$ CD11b$^+$ Gr-1$^+$. Gating strategies are presented in Figures S30 and S31.

## ■ ASSOCIATED CONTENT

### Supporting Information

The Supporting Information is available free of charge at https://pubs.acs.org/doi/10.1021/jacs.5c08583.

Oligonucleotide sequences; supplementary figures (PDF)

## ■ AUTHOR INFORMATION

### Corresponding Author

**Ying Liu** − *State Key Laboratory of Analytical Chemistry for Life Science, School of Chemistry and Chemical Engineering and Chemistry and Biomedicine Innovation Center, Nanjing University, Nanjing 210023, China;* orcid.org/0000-0001-5718-7804; Email: yingliu@nju.edu.cn

### Authors

**Shiyi Bi** − *State Key Laboratory of Analytical Chemistry for Life Science, School of Chemistry and Chemical Engineering, Nanjing University, Nanjing 210023, China*

**Ruowen Yang** − *State Key Laboratory of Analytical Chemistry for Life Science, School of Chemistry and Chemical Engineering, Nanjing University, Nanjing 210023, China*

**Yulin Cong** − *State Key Laboratory of Analytical Chemistry for Life Science, School of Chemistry and Chemical Engineering, Nanjing University, Nanjing 210023, China*

**Huangxian Ju** − *State Key Laboratory of Analytical Chemistry for Life Science, School of Chemistry and Chemical Engineering, Nanjing University, Nanjing 210023, China;* orcid.org/0000-0002-6741-5302

Complete contact information is available at: https://pubs.acs.org/10.1021/jacs.5c08583

### Author Contributions

The manuscript was written through contributions of all authors. All authors have given approval to the final version of the manuscript.

### Notes

The authors declare no competing financial interest.

## ■ ACKNOWLEDGMENTS

We gratefully acknowledge the National Natural Science Foundation of China (22374073), State Key Laboratory of Analytical Chemistry for Life Science (5431ZZXM2504).

## ■ REFERENCES

(1) Ablasser, A.; Chen, Z. J. cGAS in action: Expanding roles in immunity and inflammation. *Science* **2019**, *363* (6431), No. eaat8657.

(2) Zhu, Y.; An, X.; Zhang, X.; Qiao, Y.; Zheng, T.; Li, X. STING: a master regulator in the cancer-immunity cycle. *Mol. Cancer* **2019**, *18* (1), 152.

(3) Corrales, L.; Glickman, L. H.; McWhirter, S. M.; Kanne, D. B.; Sivick, K. E.; Katibah, G. E.; Woo, S. R.; Lemmens, E.; Banda, T.; Leong, J. J.; et al. Direct activation of STING in the tumor microenvironment leads to potent and systemic tumor regression and immunity. *Cell Rep.* **2015**, *11* (7), 1018−1030.

(4) Motwani, M.; Pesiridis, S.; Fitzgerald, K. A. DNA sensing by the cGAS-STING pathway in health and disease. *Nat. Rev. Genet.* **2019**, *20* (11), 657−674.

(5) Luo, Z.; Liang, X.; He, T.; Qin, X.; Li, X.; Li, Y.; Li, L.; Loh, X. J.; Gong, C.; Liu, X. Lanthanide-nucleotide coordination nanoparticles for STING activation. *J. Am. Chem. Soc.* **2022**, *144* (36), 16366−16377.

(6) Li, W.; Lu, L.; Lu, J.; Wang, X.; Yang, C.; Jin, J.; Wu, L.; Hong, X.; Li, F.; Cao, D.; et al. cGAS-STING−mediated DNA sensing maintains CD8$^+$ T cell stemness and promotes antitumor T cell therapy. *Sci. Transl. Med.* **2020**, *12* (549), No. eaay9013.

(7) Wang, X.; Liu, Y.; Xue, C.; Hu, Y.; Zhao, Y.; Cai, K.; Li, M.; Luo, Z. A protein-based cGAS-STING nanoagonist enhances T cell-mediated anti-tumor immune responses. *Nat. Commun.* **2022**, *13* (1), 5685.

(8) Pan, B. S.; Perera, S. A.; Piesvaux, J. A.; Presland, J. P.; Schroeder, G. K.; Cumming, J. N.; Trotter, B. W.; Altman, M. D.;

Buevich, A. V.; Cash, B.; et al. An orally available non-nucleotide STING agonist with antitumor activity. *Science* **2020**, *369* (6506), No. eaba6098.

(9) Shae, D.; Becker, K. W.; Christov, P.; Yun, D. S.; Lytton-Jean, A. K. R.; Sevimli, S.; Ascano, M.; Kelley, M.; Johnson, D. B.; Balko, J. M.; et al. Endosomolytic polymersomes increase the activity of cyclic dinucleotide STING agonists to enhance cancer immunotherapy. *Nat. Nanotechnol.* **2019**, *14* (3), 269−278.

(10) Yang, K.; Han, W.; Jiang, X.; Piffko, A.; Bugno, J.; Han, C.; Li, S.; Liang, H.; Xu, Z.; Zheng, W.; et al. Zinc cyclic di-AMP nanoparticles target and suppress tumours via endothelial STING activation and tumour-associated macrophage reinvigoration. *Nat. Nanotechnol.* **2022**, *17* (12), 1322−1331.

(11) Zhuo, S. H.; Wang, T. Y.; Zhao, L.; Su, J. Y.; Hu, J. J.; Zhao, Y. F.; Li, Y. M. piSTING: a pocket-independent agonist based on multivalency-driven STING oligomerization. *Angew. Chem., Int. Ed.* **2024**, *63* (38), No. e202407037.

(12) Skopelja-Gardner, S.; An, J.; Elkon, K. B. Role of the cGAS−STING pathway in systemic and organ-specific diseases. *Nat. Rev. Nephrol.* **2022**, *18* (9), 558−572.

(13) Van Herck, S.; Feng, B.; Tang, L. Delivery of STING agonists for adjuvanting subunit vaccines. *Adv. Drug Delivery Rev.* **2021**, *179*, No. 114020.

(14) Samson, N.; Ablasser, A. The cGAS−STING pathway and cancer. *Nat. Cancer* **2022**, *3* (12), 1452−1463.

(15) Gulen, M. F.; Koch, U.; Haag, S. M.; Schuler, F.; Apetoh, L.; Villunger, A.; Radtke, F.; Ablasser, A. Signalling strength determines proapoptotic functions of STING. *Nat. Commun.* **2017**, *8* (1), 427.

(16) Philipp, N.; Kazerani, M.; Nicholls, A.; Vick, B.; Wulf, J.; Straub, T.; Scheurer, M.; Muth, A.; Hänel, G.; Nixdorf, D.; et al. T-cell exhaustion induced by continuous bispecific molecule exposure is ameliorated by treatment-free intervals. *Blood* **2022**, *140* (10), 1104−1118.

(17) Lanng, K. R. B.; Lauridsen, E. L.; Jakobsen, M. R. The balance of STING signaling orchestrates immunity in cancer. *Nat. Immunol.* **2024**, *25* (7), 1144−1157.

(18) Weber, E. W.; Parker, K. R.; Sotillo, E.; Lynn, R. C.; Anbunathan, H.; Lattin, J.; Good, Z.; Belk, J. A.; Daniel, B.; Klysz, D.; et al. Transient rest restores functionality in exhausted CAR-T cells through epigenetic remodeling. *Science* **2021**, *372* (6537), No. eaba1786.

(19) Nguyen, N. T.; Huang, K.; Zeng, H.; Jing, J.; Wang, R.; Fang, S.; Chen, J.; Liu, X.; Huang, Z.; You, M. J.; et al. Nano-optogenetic engineering of CAR T cells for precision immunotherapy with enhanced safety. *Nat. Nanotechnol.* **2021**, *16* (12), 1424−1434.

(20) Zhang, F.; Nangreave, J.; Liu, Y.; Yan, H. Structural DNA Nanotechnology: State of the art and future perspective. *J. Am. Chem. Soc.* **2014**, *136* (32), 11198−11211.

(21) Andreeva, L.; Hiller, B.; Kostrewa, D.; Lässig, C.; de Oliveira Mann, C. C.; Jan Drexler, D.; Maiser, A.; Gaidt, M.; Leonhardt, H.; Hornung, V.; et al. cGAS senses long and HMGB/TFAM-bound U-turn DNA by forming protein−DNA ladders. *Nature* **2017**, *549* (7672), 394−398.

(22) Zhou, W.; Whiteley, A. T.; de Oliveira Mann, C. C.; Morehouse, B. R.; Nowak, R. P.; Fischer, E. S.; Gray, N. S.; Mekalanos, J. J.; Kranzusch, P. J. Structure of the human cGAS−DNA complex reveals enhanced control of immune surveillance. *Cell* **2018**, *174* (2), 300−311.e311.

(23) Morihiro, K.; Osumi, H.; Morita, S.; Hattori, T.; Baba, M.; Harada, N.; Ohashi, R.; Okamoto, A. Oncolytic hairpin DNA pair: selective cytotoxic inducer through microRNA-triggered DNA self-assembly. *J. Am. Chem. Soc.* **2023**, *145* (1), 135−142.

(24) Xu, X.; Fan, H.; Yang, Y.; Yao, S.; Yu, W.; Guo, Z.; Tan, W. Virus-like particle-induced cGAS-STING activation and AIM2 inflammasome-mediated pyroptosis for robust cancer immunotherapy. *Angew. Chem., Int. Ed.* **2023**, *62* (24), No. e202303010.

(25) Yu, F.; Li, X.; Zhao, J.; Zhao, Y.; Li, L. Photoactivated DNA assembly and disassembly for on-demand activation and termination of cGAS-STING signaling. *Angew. Chem., Int. Ed.* **2023**, *62* (33), No. e202305837.

(26) Li, X.; Yu, F.; Li, L. Tandem-controlled dynamic DNA assembly enables temporally-selective orthogonal regulation of cGAS-STING stimulation. *Angew. Chem., Int. Ed.* **2025**, *64* (7), No. e202417916.

(27) Zhao, Y.; Gao, S.; Song, D.; Ye, Z.; Xu, R.; Luo, Y.; Xu, Q. Lipidoid artificial compartments for bidirectional regulation of enzyme activity through nanomechanical action. *J. Am. Chem. Soc.* **2023**, *145* (1), 551−559.

(28) Zhao, Y.; Ye, Z.; Song, D.; Wich, D.; Gao, S.; Khirallah, J.; Xu, Q. Nanomechanical action opens endo-lysosomal compartments. *Nat. Commun.* **2023**, *14* (1), 6645.

(29) Zhang, Y.; Zhang, Y.; Song, G.; He, Y.; Zhang, X.; Liu, Y.; Ju, H. A DNA-azobenzene nanopump fueled by upconversion luminescence for controllable intracellular drug release. *Angew. Chem., Int. Ed.* **2019**, *58* (50), 18207−18211.

(30) Beharry, A. A.; Woolley, G. A. Azobenzene photoswitches for biomolecules. *Chem. Soc. Rev.* **2011**, *40* (8), 4422−4437.

(31) Kamiya, Y.; Asanuma, H. Light-driven DNA nanomachine with a photoresponsive molecular engine. *Acc. Chem. Res.* **2014**, *47* (6), 1663−1672.

(32) Dong, M.; Babalhavaeji, A.; Samanta, S.; Beharry, A. A.; Woolley, G. A. Red-shifting azobenzene photoswitches for in vivo Use. *Acc. Chem. Res.* **2015**, *48* (10), 2662−2670.

(33) Asanuma, H.; Ito, T.; Yoshida, T.; Liang, X.; Komiyama, M. Photoregulation of the formation and dissociation of a DNA duplex by using the cis−trans isomerization of azobenzene. *Angew. Chem., Int. Ed.* **1999**, *38* (16), 2393−2395.

(34) Liang, X.; Mochizuki, T.; Asanuma, H. A supra-photoswitch involving sandwiched DNA base pairs and azobenzenes for light-driven nanostructures and nanodevices. *Small* **2009**, *5* (15), 1761−1768.

(35) Yuan, Q.; Zhang, Y.; Chen, T.; Lu, D.; Zhao, Z.; Zhang, X.; Li, Z.; Yan, C.-H.; Tan, W. Photon-manipulated drug release from a mesoporous nanocontainer controlled by azobenzene-modified nucleic acid. *ACS Nano* **2012**, *6* (7), 6337−6344.

(36) Yang, Y.; Goetzfried, M. A.; Hidaka, K.; You, M.; Tan, W.; Sugiyama, H.; Endo, M. Direct visualization of walking motions of photocontrolled nanomachine on the DNA nanostructure. *Nano Lett.* **2015**, *15* (10), 6672−6676.

(37) Nakasone, Y.; Ooi, H.; Kamiya, Y.; Asanuma, H.; Terazima, M. Dynamics of inter-DNA chain interaction of photoresponsive DNA. *J. Am. Chem. Soc.* **2016**, *138* (29), 9001−9004.

(38) Ouldridge, T. E.; Sulc, P.; Romano, F.; Doye, J. P.; Louis, A. A. DNA hybridization kinetics: zippering, internal displacement and sequence dependence. *Nucleic Acids Res.* **2013**, *41* (19), 8886−8895.

(39) Zhang, X.; Chen, W.; Xie, X.; Li, Y.; Chen, D.; Chao, Z.; Liu, C.; Ma, H.; Liu, Y.; Ju, H. Boosting luminance energy transfer efficiency in upconversion nanoparticles with an energy-concentrating zone. *Angew. Chem., Int. Ed.* **2019**, *58* (35), 12117−12122.

(40) Qiu, Y.; Yang, Y.; Valenzuela, C.; Zhang, X.; Yang, M.; Xue, P.; Ma, J.; Liu, Z.; Wang, L.; Feng, W. Near-infrared light-driven three-dimensional soft photonic crystals loaded with upconversion nanoparticles. *Adv. Opt. Mater.* **2022**, *10* (9), No. 2102475.

(41) Kumar, G. S.; Neckers, D. C. Photochemistry of azobenzene-containing polymers. *Chem. Rev.* **1989**, *89* (8), 1915−1925.

(42) Du, M.; Chen, Z. J. DNA-induced liquid phase condensation of cGAS activates innate immune signaling. *Science* **2018**, *361* (6403), 704−709.

(43) Hyjek-Składanowska, M.; Vickers, T. A.; Napiórkowska, A.; Anderson, B. A.; Tanowitz, M.; Crooke, S. T.; Liang, X.; Seth, P. P.; Nowotny, M. Origins of the increased affinity of phosphorothioate-modified therapeutic nucleic acids for proteins. *J. Am. Chem. Soc.* **2020**, *142* (16), 7456−7468.

(44) Wang, Q.; Bergholz, J. S.; Ding, L.; Lin, Z.; Kabraji, S. K.; Hughes, M. E.; He, X.; Xie, S.; Jiang, T.; Wang, W.; Zoeller, J. J.; Kim, H. J.; Roberts, T. M.; Konstantinopoulos, P. A.; Matulonis, U. A.; Dillon, D. A.; Winer, E. P.; Lin, N. U.; Zhao, J. J. STING agonism

reprograms tumor-associated macrophages and overcomes resistance to PARP inhibition in BRCA1-deficient models of breast cancer. *Nat. Commun.* **2022**, *13*, 3022.

(45) Li, K.; Yu, X.; Xu, Y.; Wang, H.; Liu, Z.; Wu, C.; Luo, X.; Xu, J.; Fang, Y.; Ju, E.; Lv, S.; Chan, H.; La, Y.; He, W.; Tao, Y.; Li, M. Cascaded immunotherapy with implantable dual-drug depots sequentially releasing STING agonists and apoptosis inducers. *Nat. Commun.* **2025**, *16*, 1629.